

A Robust C-Band Hydrometeor Identification Algorithm and Application to a Long-Term Polarimetric Radar Dataset

BRENDA DOLAN AND STEVEN A. RUTLEDGE

Department of Atmospheric Science, Colorado State University, Fort Collins, Colorado

S. LIM

Korea Institute of Construction Technology, Goyang-Si Gyeonggi-Do, South Korea

V. CHANDRASEKAR AND M. THURAI

Department of Electrical and Computer Engineering, Colorado State University, Fort Collins, Colorado

(Manuscript received 8 October 2012, in final form 30 April 2013)

ABSTRACT

A new 10-category, polarimetric-based hydrometeor identification algorithm (HID) for C band is developed from theoretical scattering simulations including wet snow, hail, and big drops/melting hail. The HID is applied to data from seven wet seasons in Darwin, Australia, using the polarimetric C-band (C-POL) radar, to investigate microphysical differences between monsoon and break periods. Scattering simulations reveal significant Mie effects with large hail (diameter > 1.5 cm), with reduced reflectivity and enhanced differential reflectivity Z_{dr} and specific differential phase K_{dp} relative to those associated with S band. Wet snow is found to be associated with greatly depreciated correlation coefficient ρ_{hv} and moderate values of Z_{dr} . It is noted that large oblate liquid drops can produce the same electromagnetic signatures at C band as melting hail falling quasi stably, resulting in some ambiguity in the HID retrievals. Application of the new HID to seven seasons of C-POL data reveals that hail and big drops/melting hail occur much more frequently during break periods than during monsoon periods. Break periods have a high frequency of vertically aligned ice above 12 km, suggesting the presence of strong electric fields. Reflectivity and mean drop diameter D_0 statistics demonstrate that convective areas in both monsoon and break periods may have robust coalescence or melting precipitation ice processes, leading to enhanced reflectivity and broader distributions of D_0 . Conversely, for stratiform regions in both regimes, mean reflectivity decreases below the melting level, indicative of evaporative processes. Break periods also have larger ice water path fractions, indicating substantial mixed-phase precipitation generation as compared with monsoonal periods. In monsoon periods, a larger percentage of precipitation is produced through warm-rain processes.

1. Introduction

The Bureau of Meteorology Research Centre (BMRC) C-band polarimetric radar (C-POL) has been operating nearly continuously during every wet season in Darwin, Australia, since 1998 (Keenan et al. 1998). This long record of polarimetric observations is unique and allows for investigation of robust statistics of microphysics associated with different meteorological regimes that occur over Darwin, such as the monsoon and break periods.

A number of studies have characterized convection during the monsoon and break periods (e.g., Keenan and Carbone 1992; Rutledge et al. 1992; Keenan and Rutledge 1993; Drosowsky 1996; Cifelli and Rutledge 1998; May and Ballinger 2007; Bringi et al. 2009). Break-season convection is generally more intense, more electrically active, and more likely to have high reflectivities occurring above the freezing level and significant hail production aloft (Keenan and Carbone 1992; Mapes and Houze 1992; Rutledge et al. 1992; May et al. 2001, 2008; May and Ballinger 2007). Monsoon periods are marked by large stratiform regions with embedded convection, with significant rain accumulation due to warm-rain processes (Keenan and Carbone 1992; Rutledge et al. 1992; May and Ballinger 2007). Whereas previous studies were

Corresponding author address: Brenda Dolan, Dept. of Atmospheric Science, Colorado State University, Fort Collins, CO 80523-1371.

E-mail: bdolan@atmos.colostate.edu

mainly focused on the case-study approach with individual cases or a season of data (Thurai et al. 2010), this study goes further and uses seven seasons of polarimetric data from C-POL to investigate more broadly the microphysical differences between these regimes.

Hydrometeor identification algorithms (HID) have been widely used to investigate bulk microphysics, especially at S band (Ryzhkov et al. 2005c; Tessendorf et al. 2005; Kumjian and Ryzhkov 2008, etc.). Many of the algorithms are based on fuzzy logic methods, in which overlapping and soft boundaries can reduce the influence of noise and bias in the measurements when compared with simple lookup tables (Liu and Chandrasekar 2000; Lim et al. 2005; Ryzhkov et al. 2005c; Dolan and Rutledge 2009; Chandrasekar et al. 2013). Special consideration must be given to application of these algorithms at C- and X-band wavelengths, for which significant resonance effects and Mie scattering can lead to ambiguities in classification of different hydrometeors (Meischner et al. 1991; Zrníc et al. 2000; Keenan et al. 2001; Schuur et al. 2001; Alberoni et al. 2002; Keenan 2003; Baldini et al. 2005; Marzano et al. 2006, 2007; Kumjian and Ryzhkov 2008; Anderson et al. 2011). As described by Zrníc et al. (2000), Keenan et al. (2001), and Thurai et al. (2007), C-band resonance effects, associated with drops of 5.5–7 mm, can be especially significant in drop size distributions that result from melting precipitation ice. In addition, the effect of a quasi-stable melting hailstone with a water torus can lead to significant values of differential reflectivity Z_{dr} at C band (Meischner et al. 1991; May et al. 2001; Ryzhkov et al. 2007; Kumjian and Ryzhkov 2008; Anderson et al. 2011). Despite some of these challenges, fuzzy logic-type classification algorithms have recently been adapted to shorter wavelengths, including X band (Dolan and Rutledge 2009, henceforth DR09) and C band (Meischner et al. 1991; Zrníc et al. 2000; Keenan et al. 2001; Schuur et al. 2001; Alberoni et al. 2002; Keenan 2003; Baldini et al. 2005; Marzano et al. 2006, 2007; Keranen et al. 2007; Kumjian and Ryzhkov 2008; Anderson et al. 2011).

Although extension of the HID to C band is obvious, many of the algorithms are empirically tuned from S-band algorithms (e.g., Keenan et al. 2001; Keenan 2003; Baldini et al. 2005; Keranen et al. 2007). Anderson et al. (2011) produced a study of hail observations at C band, and a series of studies by Marzano et al. (2006, 2007) modeled 10 hydrometeor categories using T matrix to develop a fuzzy logic classification using primarily reflectivity Z_h and Z_{dr} along with temperature. We have developed a comprehensive hydrometeor identification algorithm from first scattering principles using four polarimetric radar observables (Z_h , Z_{dr} , specific differential phase K_{dp} , and correlation coefficient ρ_{hv}) along

with temperature entailing 10 different hydrometeor categories: drizzle, rain, wet snow, dry snow, ice crystals, vertically aligned ice, high-density graupel, low-density graupel, hail, and big drops (>5 mm)/melting hail. We will pay particular attention to the challenging categories of wet snow, hail, and big drops/melting hail.

Last, validation of such a hydrometeor classification algorithm is challenging because of the lack of in situ data for direct comparison. Without any data from instruments such as those on a storm-penetrating aircraft, a hydrometeor classification algorithm can only be indirectly validated by comparisons with previous research findings and conceptual models of bulk microphysics within various types of storms. Herein, we approach the problem of validation with a two-pronged approach; first, we build our hydrometeor identification algorithm from basic scattering principles and compare our results with previous research. Second, we apply the algorithm to data from the C-POL radar in Darwin, Australia, to compare results of the HID with conceptual models of bulk microphysics during the break and monsoon, providing an indirect validation. We then extend this algorithm to the full multiyear dataset from the C-POL radar to study broad microphysical differences between regimes. Although this is somewhat circular to use the C-POL data as both indirect validation of the HID and to extend our knowledge of microphysical differences between regimes, this circularity cannot be avoided without a direct method of validating HIDs.

To be able to quantitatively analyze the C-POL data in a consistent and meaningful way, significant quality control was necessary. The quality-control measures that were undertaken are described in section 2. A theoretical HID that is based on the scattering simulations of DR09 was developed. The polarimetric signatures of big drops/melting hail, wet snow, and hail along with algorithm details are provided in section 3. The results of the HID will then be used to investigate microphysical differences between the monsoon and break periods over a 7-season C-POL data record (section 4).

2. Quality control and data processing

The data used in this study represent nearly 1100 days of radar observations over seven field seasons from 1999 to 2007 (Table 1). The C-POL scanning strategy is nominally a 10-min sequence including a 17-tilt volume followed by several RHIs. Every hour, vertically pointing scans are included in the series. To develop robust statistics over the 7 yr of data, substantial quality control was necessary. This included calibration of both Z_{dr} and Z_h , attenuation and differential attenuation correction, nonmeteorological echo removal, and calculation of K_{dp} .

TABLE 1. C-POL data periods used in this study (note that during the 2000/01 wet season the C-POL radar was moved to Sydney to support the 2000 Olympic Games).

Dates	No. of C-POL obs days	Break days	Monsoon days	Transition days
4 Nov 1999–3 Apr 2000	150	71 (47%)	39 (26%)	40 (27%)
26 Oct 2001–3 May 2002	186	112 (60%)	51 (27%)	23 (12%)
1 Nov 2002–29 Apr 2003	158	92 (58%)	33 (21%)	33 (21%)
20 Oct 2003–19 Mar 2004	142	69 (49%)	49 (35%)	24 (17%)
3 Nov–26 Dec 2004; 6 Jan–6 Apr 2005	135	73 (54%)	35 (26%)	27 (20%)
10 Nov 2005–31 Mar 2006	142	70 (49%)	42 (30%)	30 (21%)
12 Oct 2006–18 Apr 2007	185	114 (62%)	30 (16%)	41 (22%)
Total	1098	601 (55%)	279 (25%)	218 (20%)

The efforts for developing consistent methods to apply to the entire dataset are described in the following sections.

a. Calibration

As mentioned above, the C-POL regular scanning strategy includes a vertically pointing scan every hour. Vertically pointing scans were used to calculate the bias in Z_{dr} . Areas in the rain region with reflectivity of less than 35 dBZ (to minimize attenuation and differential attenuation) should result in 0-dB Z_{dr} values (Gorgucci et al. 1999). Deviations from 0 dB were assumed to be the bias; these values were then averaged for each day and month (Fig. 1). The overall mean standard deviation of individual values from the hourly calculation is 0.13 dB, which is close to the 0.1-dB accuracy that is considered to be necessary for accurate quantitative analysis using Z_{dr} (Sachidananda and Zrnica 1987; Ryzhkov et al. 2005a). These values were also compared with seasonal values provided by the BMRC for the 2005–07 periods and were within 0.28 dB of those values. These differences are likely due to the method of calculating the biases, including the time period over which the biases are calculated (daily/monthly vs seasonal). BMRC differential reflectivity biases were calculated using $Z-Z_{dr}$ scattergrams in comparison with theoretical curves that were based on disdrometer data after reflectivity biases were calculated from comparisons with other sources (disdrometer, 35-GHz radar, and *CloudSat* profiles; A. Protat 2009, personal communication).

Once the differential reflectivity was corrected for biases, self consistency was used to calculate the reflectivity bias (Gorgucci et al. 1992, 1999, 2006; Goddard et al. 1994; Ryzhkov et al. 2005a; Bringi et al. 2006) by using

$$K_{dp}/Z_{h,lin} = 3.9610^{-5} Z_{dr}^{-0.0218} - 3.2 \times 10^{-6}, \quad (1)$$

where $Z_{h,lin}$ is the reflectivity in linear units and Z_{dr} is in decibels. Differential phase K_{dp} is iteratively calculated using (1) for synthetic values of Z_h from -20 to 30 dBZ

(representing the possible offset values) in 0.1-dB increments for raining points. The value of Z_h that yields the best match between calculated K_{dp} and measured K_{dp} provides the offset value for Z_h . The coefficients in (1) were derived using disdrometer data from the Tropical Warm Pool International Cloud Experiment (TWP-ICE) campaign in 2006 (May et al. 2008). TWP-ICE was carried out in January and February of 2006 at Darwin. Measured K_{dp} was derived using Wang and Chandrasekar (2009). As with differential reflectivity, both daily and monthly mean biases were calculated. The mean standard deviation of the daily reflectivity offsets from the monthly offset is 0.90 dBZ, which is within the 1 dBZ that has been suggested as necessary for quantitative use of reflectivity data (Sachidananda and Zrnica 1987; Ryzhkov et al. 2005a). The monthly biases calculated using the self-consistency method were generally within 1.3 dBZ of the seasonal values given by BMRC (Fig. 1). Again, differences may be due to the method applied for the bias calculation and the time frame over which the biases were calculated.

b. Attenuation correction

Specific attenuation and differential attenuation can be difficult problems when C-band radar data are being analyzed. We adapted the bulk method of attenuation correction outlined in Carey et al. (2000, henceforth C00), which uses rain-only regions to adaptively derive the coefficients between specific and differential attenuation to the specific differential phase shift by assuming a linear relationship between attenuated reflectivity and differential phase shift:

$$A_h \approx aK_{dp} \quad \text{and} \quad (2)$$

$$A_{hv} \approx bK_{dp}. \quad (3)$$

As with C00, the data were restricted to eliminate or at least to minimize Mie-scattering resonance and to ensure a linear relationship between specific differential

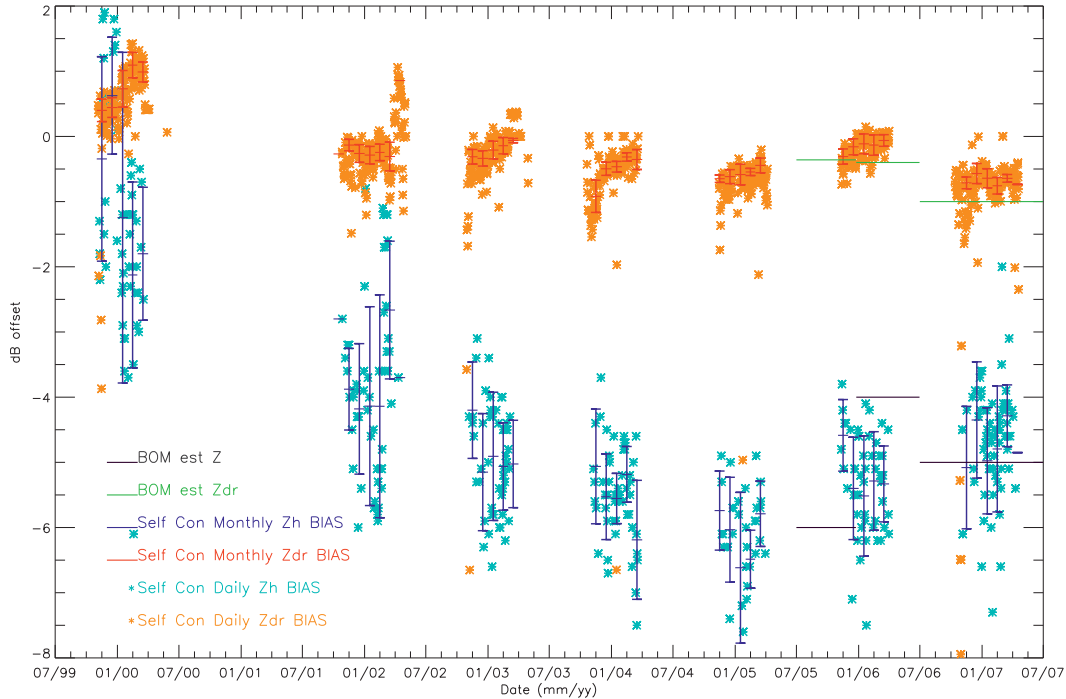


FIG. 1. Calibration estimates for Z_h and Z_{dr} for the period from October 1999 through May 2007. Daily (monthly) averages of Z_{dr} bias are shown in orange (red). Daily (monthly) averages of reflectivity bias are shown in light blue (dark blue). Error bars represent the standard deviation between the monthly mean and the daily mean. Black (green) lines represent values provided by the Bureau of Meteorology for Z_h (Z_{dr}) bias.

phase and specific attenuation A_h and specific differential attenuation A_{hv} while maintaining enough points for statistical robustness. Data were restricted to $1.0 \leq K_{dp} \leq 2.0^\circ \text{ km}^{-1}$, $Z_h < 60.0 \text{ dBZ}$, and heights between 0.5 and 2.5 km to ensure rain-only points (similar to C00). Data were further restricted recursively as with C00 until the correlation was greater than 0.9 and the number of points remained greater than 500. Then a linear regression was performed to calculate the slope, giving the a (b) coefficient for the relationship between A_h (A_{hv}) and K_{dp} . The representativeness of the calculated slope was determined by comparison with default values that were calculated by taking the mean and standard deviation of initial a and b values over the 7-yr period. The default coefficients were defined as $a = 0.08$ and $b = 0.009$, which are similar to C-band values given in Bringi et al. (1990) and C00. If the calculated slope was not within 0.03 (0.009) of the default a (b) value, then the default value was used. This procedure was to ensure that largely anomalous values did not propagate through to the attenuation correction. A correction for large drops was applied as in C00. For this dataset, large-drop regions were identified by low ρ_{hv} (< 0.8) and large K_{dp} (> 1.0) at low levels (height $< 5.0 \text{ km}$), and data were corrected using enhanced coefficients $a^* = 0.13$ and $b^* = 0.05$ (from C00 scattering simulations) in

a piecewise manner in all subsequent gates behind identified large-drop regions.

c. Data processing

Data were gridded to a Cartesian coordinate system using the National Center for Atmospheric Research “Reorder” software package. Data were gridded to 2-km resolution in the horizontal plane out to 100 km and from 0 to 20 km in the vertical direction with a 1-km resolution.

A number of methods to exploit the information contained in the polarimetric observations for improved rainfall R estimation have been developed (e.g., Cifelli et al. 2002, 2011; Ryzhkov et al. 2005b; Bringi et al. 2009). For this study, several methods were tested, and it was found that a simple algorithm that is based on hydrometeor identification and uses $Z-R$ and $R-K_{dp}$ relationships from Bringi et al. (2009) resulted in the lowest root-mean-square error and normalized bias when compared with Joss–Waldvogel disdrometer (JWD) observations of total daily accumulated rainfall during TWP-ICE (Fig. 2). Figure 3 shows the flowchart for the rainfall estimation algorithm.

Bringi et al. (2009) developed a fit between C-POL observed Z_{dr} and mean drop diameter D_0 using disdrometer

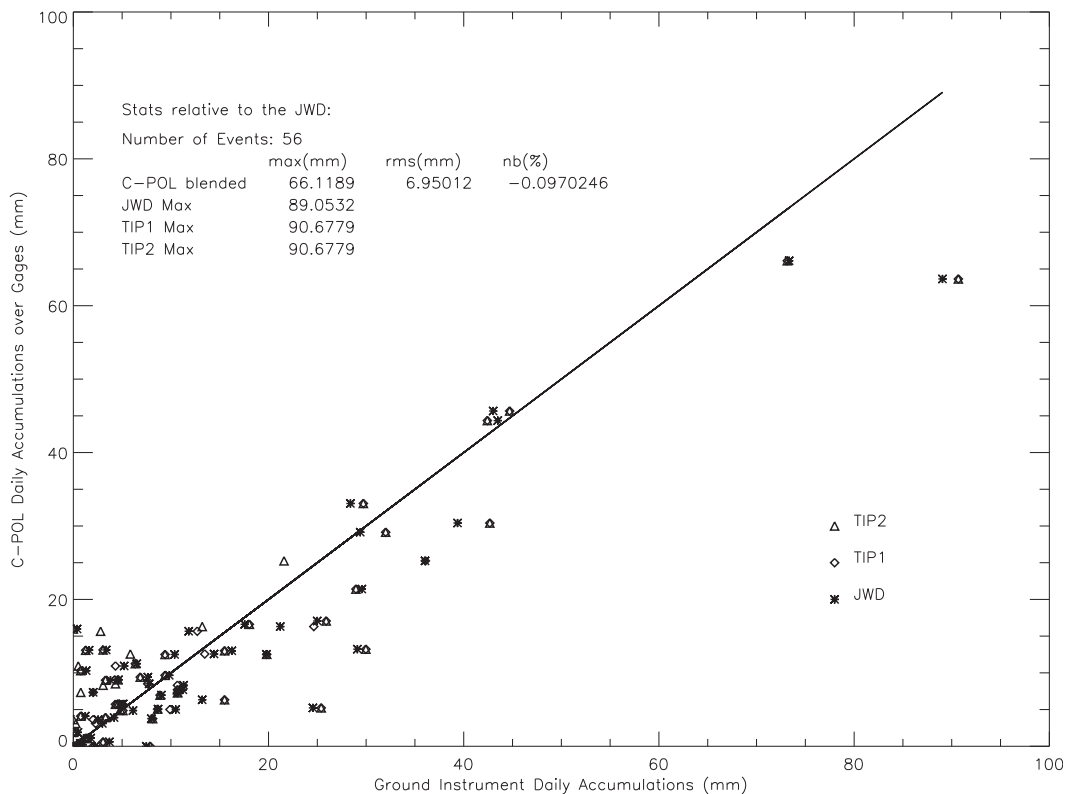


FIG. 2. C-POL-derived daily rainfall accumulations over the ground instrument site grid point with the JWD and tipping-bucket rain gauge total daily rainfall for January–February 2006 during TWP-ICE.

data. This relationship is a polynomial fit that depends on the value of Z_{dr} :

$$D_0 = 0.0203Z_{dr}^4 - 0.1488Z_{dr}^3 + 0.2209Z_{dr}^2 + 0.5571Z_{dr} + 0.801 \quad \text{for } -0.5 \leq Z_{dr} < 1.25 \text{ dB} \quad \text{or} \quad (4)$$

$$D_0 = 0.0355Z_{dr}^3 - 0.3021Z_{dr}^2 + 1.0556Z_{dr} + 0.6844 \quad \text{for } 1.25 \leq Z_{dr} < 5 \text{ dB}. \quad (5)$$

We employed the above relationships in our own study. To examine ice and rain contents and differences between break and monsoon conditions, ice and water contents were calculated from assumed relationships with reflectivity (Carey and Rutledge 2000; Cifelli et al. 2002; Lang et al. 2010). The relation for water mass is

$$M_w = 3.44 \times 10^{-3} Z_{h,rain}^{0.5714}, \quad (6)$$

where $Z_{h,rain}$ is the contribution to the reflectivity from the rain-only portion of the volume determined by using the difference reflectivity Z_{dp} . For ice water mass,

$$M_i = 1000\pi\rho_i N_0^{0.4286} (5.28 \times 10^{-18} Z_{h,ice})^{0.5714}, \quad (7)$$

and similarly $Z_{h,ice}$ is the contribution of ice to the total reflectivity determined from Z_{dp} . The density of ice ρ_i is set at 0.917 g cm^{-3} and N_0 is the intercept parameter ($4 \times 10^6 \text{ m}^{-4}$), where an inverse exponential relationship for ice has been assumed. The value of N_0 comes from a modeling study over the Tiwi Islands (Petersen 1997).

The Steiner et al. (1995) partitioning method was applied to separate echoes into stratiform and convective components. A convective-core reflectivity threshold of 40 dBZ was used, and convective centers were identified using the same peakedness criteria as in Steiner et al. [1995, their Eq. (2)], which were developed for a case in Darwin. The values were tested and found to perform well for our Darwin dataset.

3. The theoretically based C-band hydrometeor identification algorithm

Hydrometeor identification using fuzzy logic allows for determination of bulk microphysics within a given radar volume (Liu and Chandrasekar 2000; Ryzhkov et al. 2005c; Chandrasekar et al. 2013). Membership beta functions are defined for each hydrometeor type and each variable: Z_h , Z_{dr} , K_{dp} , and ρ_{hv} . In addition to the

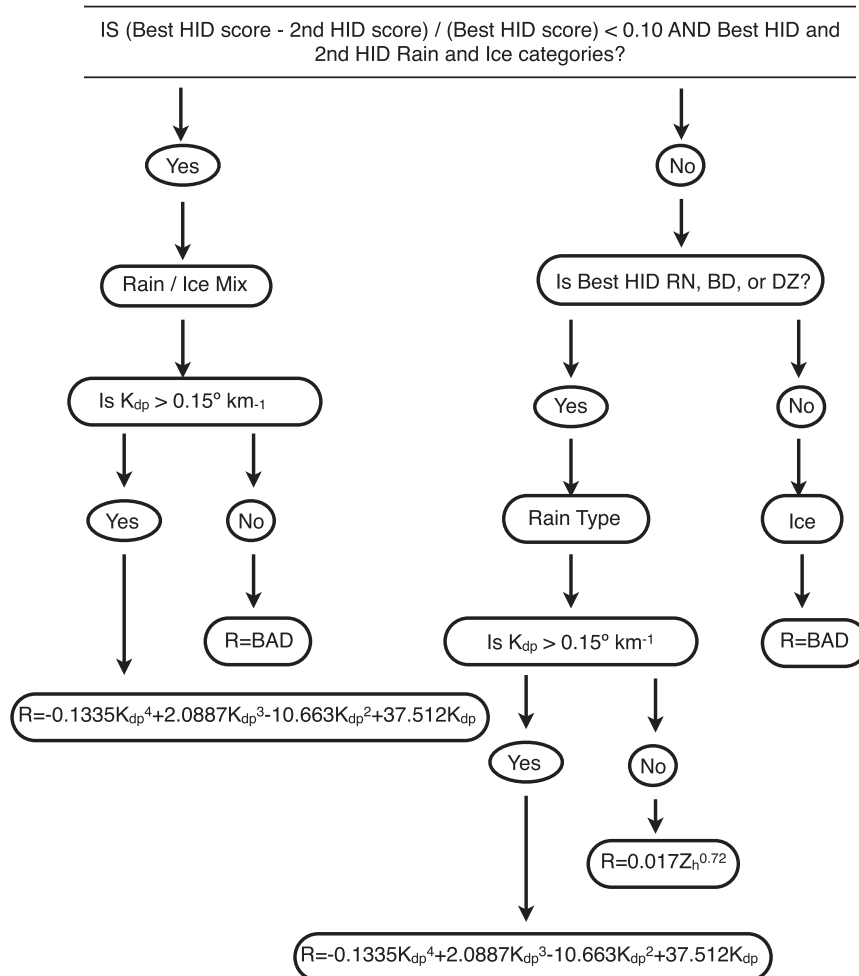


FIG. 3. Flowchart for C-POL blended rainfall estimation. Rainfall relationships are from Bringi et al. (2009).

radar observations, temperature is an important variable in the hydrometeor classification. Temperature T was derived from the nearest (in time) Darwin (“YPDN”) sounding for each C-POL volume. As with DR09, the hydrometeor with the highest fuzzy logic score was identified as the most probable type at each grid point. The algorithm uses beta functions as defined in DR09’s Eq. (14). Subjectively determined weights W are applied to K_{dp} (1.0), Z_{dr} (0.8), and ρ_{hv} (0.1) on the basis of the confidence in the measurements, and the score is multiplied by the score for Z_h and T , effectively weighting these two variables the most. The overall score μ for a given hydrometeor i is calculated with

$$\mu_i = \left[\frac{(W_{Z_{dr}} \beta_{Z_{dr},i} + W_{K_{dp}} \beta_{K_{dp},i} + W_{\rho_{hv}} \beta_{\rho_{hv},i})}{W_{Z_{dr}} + W_{K_{dp}} + W_{\rho_{hv}}} \right] \beta_{T,i} \beta_{Z_h,i}, \tag{8}$$

where i indicates the hydrometeor category, W is the weight for each variable, and β is the score from DR09’s Eq. (14) for a given hydrometeor and variable set.

In the current study, the hydrometeor identification scheme described in DR09 was adapted for C band by conducting scattering simulations for the seven categories [drizzle (DZ), rain (RN), ice crystals (IC), dry snow (DS), low-density graupel (LDG), high-density graupel (HDG), and vertically oriented ice (VI)] using a wavelength of 5.5 cm. All categories were simulated exactly as in DR09, except for vertically aligned ice. Carey et al. (2009) argue that the dispersion of canting angles for ice crystals such as needles and columns is very low when electric fields act to align the crystals. Furthermore, Carey et al. (2009) allowed larger particle sizes relative to those in DR09, resulting in much lower K_{dp} values (down to $-1.5^\circ \text{ km}^{-1}$) than were produced by DR09. The new parameters used for VI are shown in

TABLE 2. Simulation parameters for vertical ice, hail, big drops/melting hail, and wet snow. All combinations of all parameters were modeled for a given hydrometeor type, except that in the case of hail and big drops/melting hail D_0 and N_0 were simulated as pairs (for hail 0.3 and 50 000, 0.35 and 4000, . . . , 0.7 and 800; for big drops/melting hail 0.35 and 1000, 0.45 and 1000, 0.55 and 500, and 0.65 and 500). Here, for wet snow, snow rate (SR) is the water equivalent precipitation rate (mm h^{-1}).

	Axis ratio	$D_{\min}; D_{\max}; \Delta D$ (cm)	T (°C)	Air/ice bulk density (g cm^{-3})	Vol fraction of water in inner sphere	Water coat thickness (cm)	D_0 (cm)	N_0 ($\text{cm}^{-1} \text{m}^{-3}$)	Std dev canting angle (°)	Elev angle (°)
Vertical ice	0.125; 0.15; 0.35	0.005; 0.15; 0.005	-40	0.4; 0.9	—	—	0.03; 0.06; 0.07	2 000 000; 1 200 000; 40 000	1.0; 4.0 (mean: 90°)	30.0
Hail	0.6; 0.8; 1.1; 1.3	0.5; 5.0; 0.1	-5	0.7; 0.8; 0.917	0.3; 0.25	0.02; 0.25D	0.3; 0.35; 0.4; 0.45; 0.5; 0.7	50 000; 4000; 3000; 2000; 1000; 800	60; 75; 89; 95	4.3
Big drops/ melting hail	0.6; 0.7; 0.8	0.5; 1.4; 0.1	5; 20,	1	—	—	0.35; 0.45; 0.55; 0.65	1000; 1000; 500; 500	4	1; 5.0; 15.0
Wet snow	0.3; 0.5; 0.7	0.05; 1.2; 0.05	5; -10	0.2; 0.3	0.3; 0.0	0.3D	Gunn and Marshall (1958): $D_0 = 0.14\text{SR}^{0.45}$; $N_0 =$ $(2.5 \times 10^3)\text{SR}^{-0.94} \times 10$; SR: 0.05, 0.1, 0.5, and 2.5	45; 60	45; 60	5.0

Table 2. The resulting variable ranges, used to define the membership beta functions, are included in the appendix. Three additional categories not included in the DR09 scheme were identified as being important to studying the microphysics over Darwin. Those categories are hail, wet snow, and so-called big drops/melting hail. The input parameters for these categories are shown in Table 2. The reasoning behind the parameter selections is discussed in the following sections.

Several studies by May et al. have shown significant hail cores that are associated with intense break convection in Darwin (May et al. 2001, 2002; May and Keenan 2005). As such, it is an important category to include when analyzing the microphysics of break and monsoon convection. Hail can have complicated polarimetric signatures at C band because of Mie-scattering effects, which will be examined in the following section. In general, hail is thought to produce near-zero differential reflectivity signatures because of its randomly tumbling nature (Straka et al. 2000; Ryzhkov et al. 2005c). Several studies have found that anomalously high Z_{dr} can be associated with hail (Meischner et al. 1991; Ryzhkov et al. 2007; Kumjian and Ryzhkov 2008; Anderson et al. 2011; Kaltenboeck and Ryzhkov 2013), however, and, in particular, significant Z_{dr} enhancements at C band. Anderson et al. (2011) suggested that such high Z_{dr} signatures can be explained by melting hail. The meltwater is assumed to be confined in a torus, which greatly reduces the tumbling nature of hail, yielding small canting angles and subsequently large Z_{dr} values. Thus, this process can have polarimetric signatures that are very similar to those of large drops, with high Z_{dr} values and moderate to high K_{dp} values, as well as reduced ρ_{hv} because of melting and ice/water mixtures. In addition, ρ_{hv} is lowered because of resonance effects in both melting hail and large drops. It may be beyond the capability of polarimetric radar to distinguish a melting hail particle with a significant water torus from a large, oblate, mostly water target with an ice core or a large all-water drop that has formed through collision-coalescence processes. As such, we will consider a single big drop/melting hail category that attempts to encompass these processes. Last, a wet snow category is important for identifying the melting layer and is generally associated with stratiform precipitation as aggregates melt into raindrops. Although this creates a very distinct brightband signature (e.g., Zrníc et al. 1993a; Ryzhkov et al. 2005b), it can result in complicated Mie-scattering effects at C band as the large aggregates become wetted.

a. Hail

To model properly the scattering properties of hail (including both dry and wet growth conditions; melting

hail will be discussed below), a two-layer T matrix was implemented by following the method of Depue et al. (2007). Size ranges from 0.5 to 5 cm were utilized. Knight (1986) found that the axis ratio of hail can range from 0.6 to 1.0. One limitation of the T-matrix model is the assumption that the particles are spheroids. Since hailstones are known to have irregularities such as protrusions or spikes, we have attempted to account for various shapes by selectively varying the axis ratio, allowing it to exceed 1.0 to simulate a prolate appearance. This is similar to the method of Russchenberg and Ligthart (1996) to approximate the random particle motions of melting snowflakes using variations in the canting angles. Two thicknesses of water coatings were used: one with a constant 0.02-cm coating and one with a water-coat thickness equivalent to 25% of the particle's diameter. For particles smaller than 2 cm, a 25% water coating is 0.5 cm or less, which is below the C-band threshold thickness for which a particle appears to the radar as an all-water target (Battan 1979). This means that we are capturing some of the erratic Mie-scattering behavior of hail at C band. Hail was also modeled without a water coating to simulate "dry hail." The density of the inner ice shell was modeled using that of ice (0.917 g cm^{-3}) as well as 0.7 and 0.8 g cm^{-3} to simulate slightly less dense, more spongy hail (Depue et al. 2007). The canting angle of falling hail is still relatively unknown. List et al. (1973) found that hail falls with its major axis horizontal, whereas studies by Zrníc et al. (1993b) found that the major axis was aligned in the vertical direction. Knight and Knight (1970) argue that hail tumbles as it falls, with large, random canting angles, resulting in isotropic scattering leading to near-zero values of differential reflectivity. Rasmussen and Heymsfield (1987a), however, argued that, as hail falls, the outer water collects into a torus around the major axis and the hail falls much more stably. Studies by Anderson et al. (2011) suggest that this arrangement explains high Z_{dr} values associated with hail observations at C band (Meischner et al. 1991; Ryzhkov et al. 2009; Tabary et al. 2009; Anderson et al. 2011; Kaltenboeck and Ryzhkov 2013). They found that these circumstances occurred well below the melting layer and that hail near the melting layer was still associated with near-zero Z_{dr} , suggesting isotropic scattering associated with significant tumbling. We will consider the "hail" category to be associated with tumbling hail with a quasi-uniform distribution of water around an ice core, and we will consider hail with a significant water torus that falls more stably to be "melting hail," which will be considered as a separate category (see below). For this reason, large canting angles were used to simulate hail. Cheng and English (1983) and Ryzhkov et al. (2009) found

exponential distributions of hail. The Cheng and English (1983) exponential distribution can be described with a slope parameter Λ that is related to the number distribution through

$$N(D) = 115\Lambda^{3.63} \exp(-\Lambda D), \quad (9)$$

where D is diameter and Λ is related to the median diameter D_0 ; D_0 was calculated using $D_0 = 3.67\Lambda^{-1}$ (Ulbrich 1983). A summary of the hail microphysical parameters that were modeled for this study is given in Table 2, and the resulting simulated polarimetric ranges and membership beta function values are given in the appendix.

Hail with the assumed parameters was also modeled using a wavelength of 11 cm to provide a baseline for the C-band simulations since S band is less susceptible to Mie effects. Simulated S-band values were compared with a number of sources (Straka et al. 2000; Tessoroff et al. 2005) and were thus determined to be physically representative of hail, lending confidence to the microphysical parameters used in the simulations. To illustrate the nonlinear effects, polarimetric observations for the 0.2-mm water coat for a monodisperse population of hailstones are shown in Fig. 4, as a function of diameter. Mie effects are noted at C band, beginning at 2.5–3 cm in diameter. Most notable is that an oscillatory behavior in reflectivity with a minimum value at 3-cm diameter is apparent. Reflectivities for diameters exceeding 2 cm are generally below those at the more well-behaved S band, while Z_{dr} and K_{dp} are significantly more negative (because of the large canting angles and prolate axis ratios used) in comparison with S-band values. The results are similar to those found for hail at C band by Marzano et al. (2007).

b. Big drops/melting hail

Under favorable conditions, large precipitation ice particles such as graupel or hail can entirely melt, forming extremely large (5–8 mm) oblate drops, resulting in a size distribution that is characterized by a few large drops mixed with small drops. Using the Rasmussen and Heymsfield (1987a) melting model, at 100% humidity, hailstones with initial sizes of 1 cm would completely melt into large water drops (~ 9 mm) after 2 km of fall (Rasmussen and Heymsfield 1987b); smaller hailstones would melt in shorter fall distances but could still produce large drops (> 5 mm). C00 speculate that the tropics may also support the development of large drops through robust coalescence that allows growth to giant drop sizes without the presence of smaller raindrops with which to collide and break up. The presence of such large drops (produced through melting or coalescence)

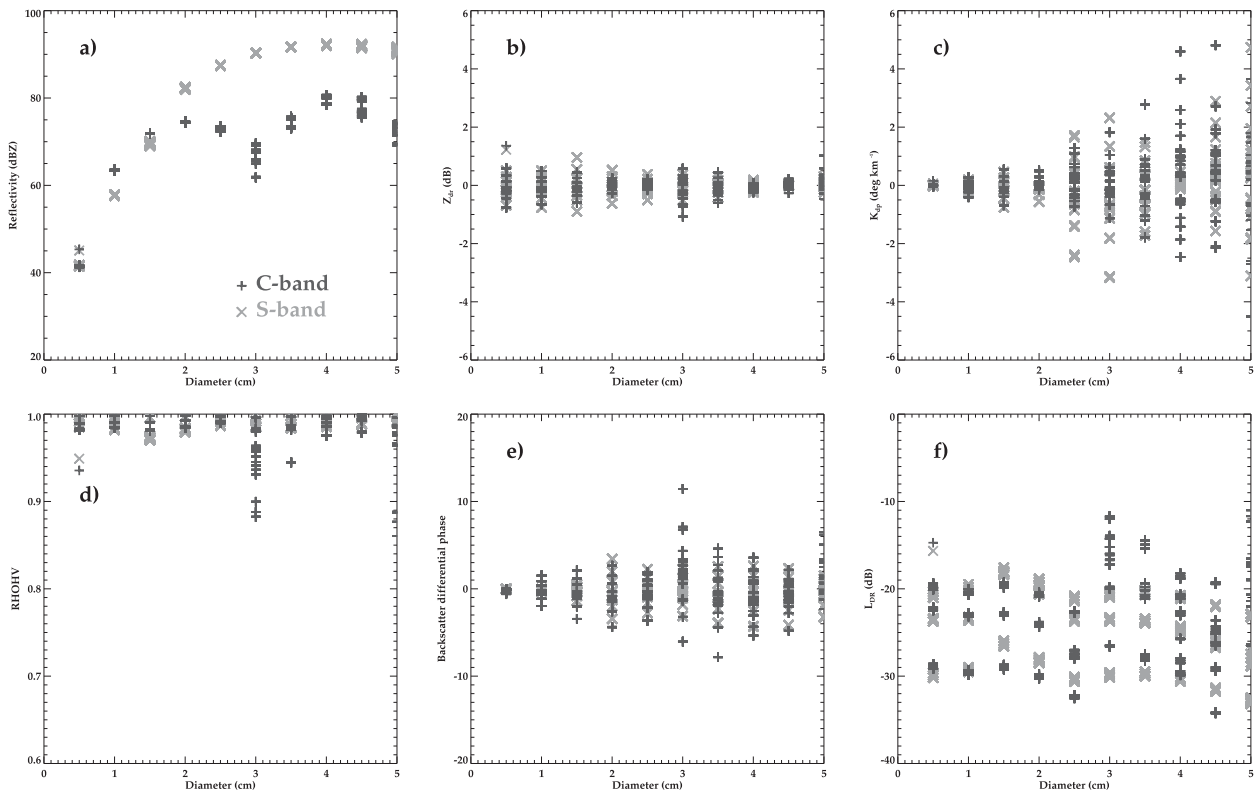


FIG. 4. Simulated radar observations: (a) reflectivity, (b) Z_{dr} , (c) K_{dp} , (d) ρ_{hv} at zero lag, (e) backscattering differential phase δ , and (f) linear depolarization ratio L_{DR} for hail as a function of hail diameter for water-coated hail (0.2 mm) for S band (gray \times s) and C band (black plus signs). Simulation parameters are given in Table 2.

dominates power-based radar returns such as reflectivity and differential reflectivity. These types of drops have been noted in a number of previous studies (Brangi et al. 1991; Meischner et al. 1991; Ryzhkov and Zrnica 1995; Keenan et al. 1998; Zrnica et al. 2000; Schuur et al. 2001; Ryzhkov et al. 2005c; Thurai et al. 2007; Kumjian and Ryzhkov 2008) and specifically over the Darwin region by C00. This can be indicative of specific microphysical conditions and can be useful for forecasting purposes (Ryzhkov et al. 2005c; Kumjian and Ryzhkov 2008; Park et al. 2009). Schuur et al. (2001) and Ryzhkov et al. (2005c) attribute these big-drop regions to either melting hail or coalescence growth in the convective updraft that can reach the ground before breaking up, and Kumjian and Ryzhkov (2008) suggest regions of large drops could be due to a size-sorting mechanism. Keenan et al. (1998) suggest that large drops are a common occurrence in the tropics.

Several authors have associated similar polarimetric signatures with melting hail below the 0°C level (Meischner et al. 1991; Ryzhkov et al. 2007, 2009; Tabary et al. 2009; Anderson et al. 2011). As discussed earlier, such hail is thought to form a significant water

torus, resulting in a more stable fall orientation for the stones, allowing for large differential signals in both power and phase. These conditions produce large Z_{dr} returns, particularly at C band, and can have somewhat reduced ρ_{hv} , along with moderate K_{dp} signatures. Earlier studies showed that C-band Z_{dr} values in hail can be on the order of 3–6 dB (Meischner et al. 1991; Ryzhkov et al. 2007, 2009; Tabary et al. 2009; Anderson et al. 2011), and some observations have found larger values, up to 8–10 dB (Anderson et al. 2011). Picca and Ryzhkov (2012) argue that hail is often mixed with rain, and wavelength effects can be large for melting hail, resulting in large Z_{dr} values. In fact, large drops and stably falling melting hail would produce very similar electromagnetic signatures and may not be distinguishable by the radar. In addition, these two hydrometeor types go hand in hand; as the hailstone continues to melt and the water coating gets thicker, it will eventually appear as an all-water target to the radar despite the possibility of a small ice core remaining (Battan 1979). Therefore for the purpose of this study, we have combined the two hydrometeor types into a single category that is characterized by large, flattened particles with a significant

amount of water, relatively small canting angles, and distributions that are similar to hail or graupel distributions.

To model this category for C-band application, which may have large resonance effects, small concentrations of large particles (similar to hail distribution) with entirely liquid, quasi-oblate particles were simulated. The parameters used for simulating big drops are given in Table 2. C-band polarimetric values are provided in the appendix. Differential reflectivity values range from 2.5 to 6.3 dB, falling into the same interval as noted in previous C-band studies of melting hail (Meischner et al. 1991; Ryzhkov et al. 2007, 2009; Tabary et al. 2009; Anderson et al. 2011). The K_{dp} values are 0.1° – $6.7^{\circ} \text{ km}^{-1}$, and reflectivities are relatively large—from 49 to 63 dBZ.

c. *Wet snow*

Another important category that was not included in DR09 is wet snow. While wet snow is relatively easy to identify at S band (Ryzhkov et al. 2005c and others), nonlinear Mie effects can be significant at shorter wavelengths. To be specific, Z_{dr} and K_{dp} can become extremely large and erratic because of Mie scattering of such sizable, water-coated hydrometeors. To explore C-band polarimetric measurements of wet snow, again the two-layer T matrix was used, following the method of Depue et al. (2007). Microphysical parameters similar to those of dry aggregated snow in DR09 were used, but with a water coating of 30% to simulate wetted, melting aggregates. Although this is a somewhat simplified model of melting as compared with more detailed studies on the melting of snow (e.g., Russchenberg and Ligthart 1996; Fabry and Szyrmer 1999), we feel it is a sufficient model for characterizing the bulk radar signatures that are associated with wet snow. This set of parameters (Table 2) resulted in moderate reflectivities (0–40 dBZ), high Z_{dr} values (0.5–2.0), small K_{dp} (-0.1° – $0.7^{\circ} \text{ km}^{-1}$), and low values of ρ_{hv} (>0.55). Specific variable ranges are provided in the appendix. As with the big drops/melting hail category, simulations were compared with values from a well-developed S-band algorithm, as well as with results from Straka et al. (2000). The S-band values fall within the range of previous S-band observations and algorithms.

4. Microphysics of the monsoon and break periods

Two distinct meteorological regimes occur within the so-called wet season in the Darwin region: “break” periods and “monsoon” periods (Keenan and Carbone 1992; Rutledge et al. 1992; Keenan and Rutledge 1993; Drosowsky 1996; May and Ballinger 2007; Bringi et al. 2009). The wet season generally lasts from about

November through April. As described by Drosowsky (1996), there are a number of methods for identifying monsoon and break periods using a variety of parameters, from rainfall to winds to large-scale circulation patterns. Herein, we use a simple definition that is based on low-level winds (Holland 1986; Hendon and Liebmann 1990), whereby a sustained mean 850-hPa zonal wind of greater than 2 m s^{-1} is defined as the monsoon and a sustained mean 850-hPa zonal wind of less than -2 m s^{-1} is labeled as a break period. Mean horizontal wind flow at 850 hPa was derived from the Modern-Era Retrospective Analysis for Research and Applications (MERRA) reanalysis data with a $2^{\circ} \times 2^{\circ}$ box centered on the C-POL radar location. The horizontal wind had to remain above or below the threshold for a minimum of 24 h to be classified as one regime versus another. Figure 5 shows the resulting regimes for the seven seasons from 1999 to 2007. The classification resulted in 601 break days, 279 monsoon days, and 218 transitional days (on which the winds were less than $|2| \text{ m s}^{-1}$). Herein, we will only examine the monsoon and break periods.

As described by Keenan and Carbone (1992), Rutledge et al. (1992), May and Ballinger (2007), and others, break convection tends to be more intense and vertically developed, with larger reflectivities above the melting layer and generally higher echo-top heights in comparison with monsoon periods, which have widespread stratiform components with embedded convection. As documented by Keenan and Carbone (1992) and Rutledge et al. (1992), break convection tends to have vigorous updrafts that promote robust mixed-phase regions, characteristics that lead to significant electrification and lightning-flash rates. May et al. (2001) and May and Keenan (2005) found significant hail cores with 1–2-cm hail associated with break convection. Large hail was found aloft, but indications of melting hail were found down to 2 km. Hail during the monsoon cases was rare.

Two examples of typical break convection are shown in Figs. 6 and 7 from 0710 UTC 15 December 2006 and 2000 UTC 15 November 2002, respectively. Examples of monsoon convection are illustrated in Figs. 8 and 9 from 1820 UTC 15 March 2006 and 1600 UTC 12 January 2003, respectively. It is clear that the break cases are characterized by stronger convection when compared with the monsoon cases, which have large regions of stratiform with embedded convective cells. Low-level plan position indicators (PPIs) of Z_{dr} on 15 December 2006 show much larger isolated pockets of enhanced Z_{dr} during the break case (indicating larger, more oblate drops or melting hail; Fig. 6), whereas the monsoon Z_{dr} values on 15 March 2006 remain generally below 2 dB with limited horizontal variability (Fig. 8). A second example of break convection from 2000 UTC 15 November

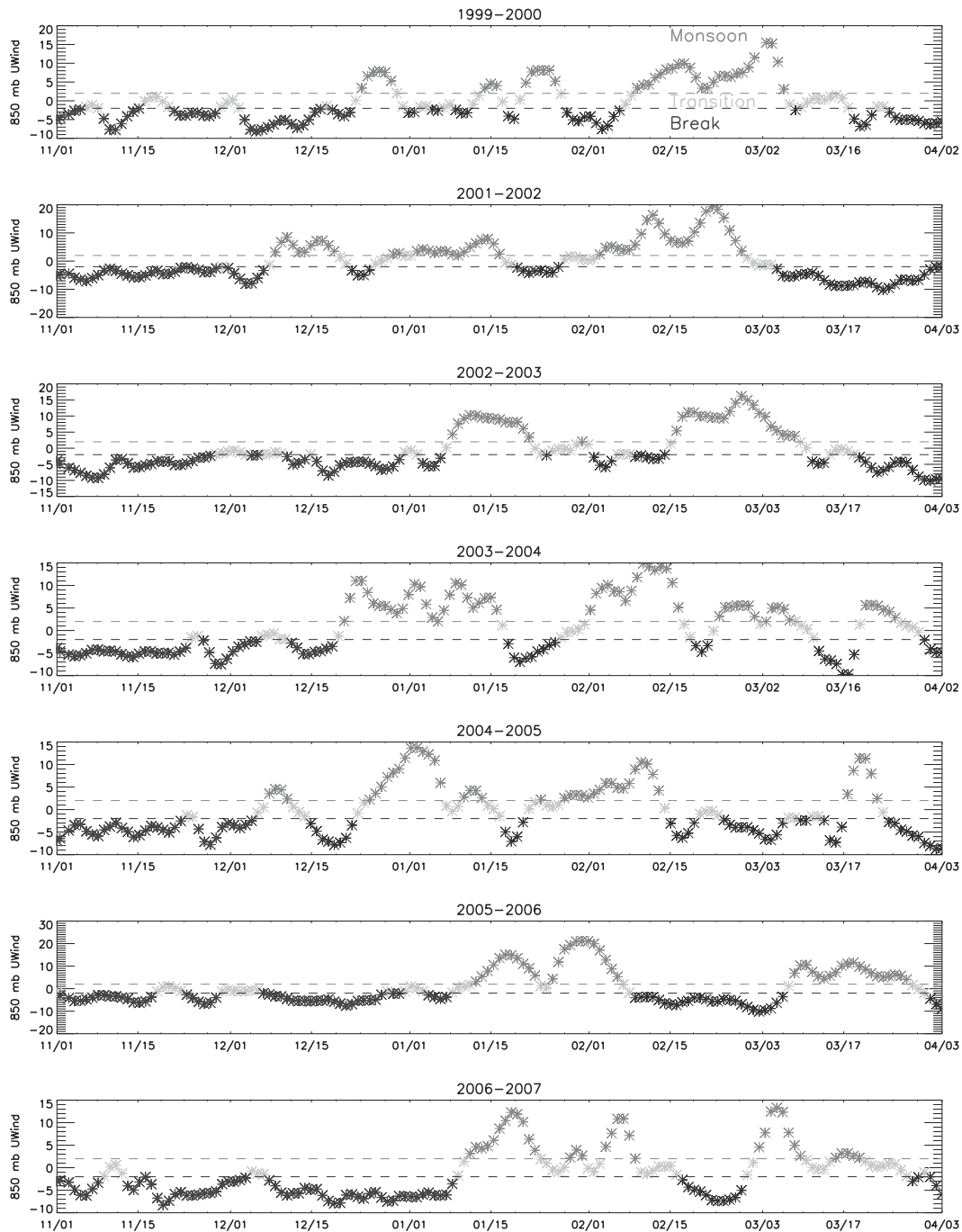


FIG. 5. Monsoon and break periods defined by the 850-hPa zonal wind from MERRA reanalysis data for the seven wet seasons (shown from November through March) analyzed herein. Positive values of U (zonal) wind (highlighted in medium gray) correspond to monsoon periods, and negative values of U wind (highlighted in black) are associated with break periods.

2002 (Fig. 7) shows more widespread intense convection when compared with the first break example (Fig. 6). Most notable is that there are large areas with greater than 50 dBZ at low levels. Significant phase shifts, indicating the presence of large amounts of liquid water, are seen in

the most intense cores, with localized K_{dp} values exceeding $9^{\circ} \text{ km}^{-1}$. Figure 9 illustrates a more intense monsoon example from 1600 UTC 12 January 2003. A large area of moderate reflectivities (>40 dBZ) is apparent, as well as large areas of stratiform (reflectivities < 30 dBZ).

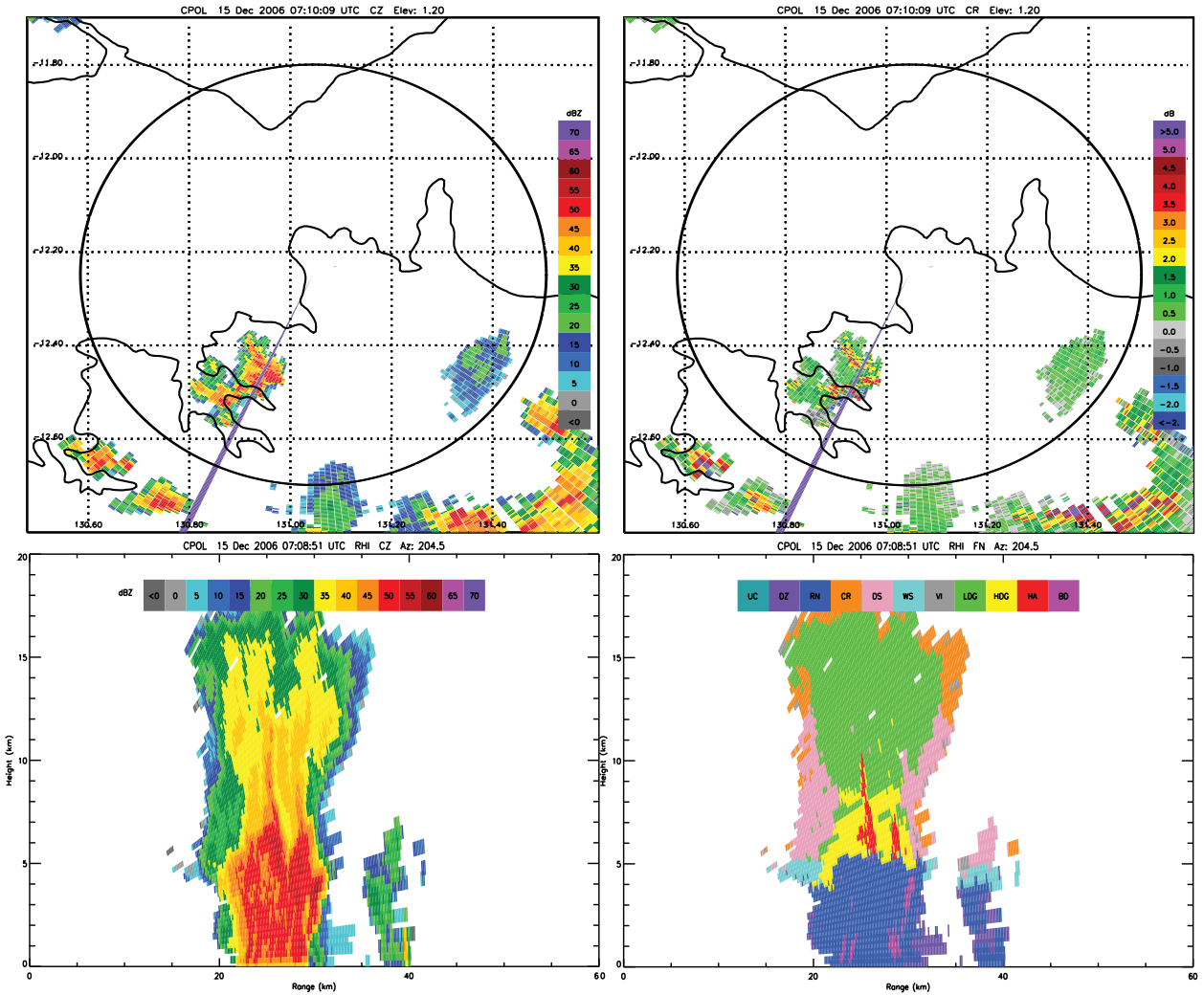


FIG. 6. Example of typical break convection from 0710 UTC 15 Dec 2006: (top left) reflectivity and (top right) Z_{dr} PPIs and (bottom left) reflectivity and (bottom right) HID RHIs along 204° azimuth (illustrated by purple ray in the top panels). HID categories are defined as (from left to right in the bottom-right color bar) UC = unclassified, DZ = drizzle, RN = rain, CR = ice crystals, DS = dry snow, WS = wet snow, VI = vertical ice, LDG = low-density graupel, HDG = high-density graupel, HA = hail, BD = big drops/melting hail.

A relatively widespread region of moderate K_{dp} ($4\text{--}7^\circ \text{ km}^{-1}$) accompanies the convective areas, demonstrating the presence of widespread liquid water at low levels (Fig. 9). Although the surface values are not as large as in the 15 November 2002 break case, the horizontal extent of moderate K_{dp} is larger during this monsoon case.

A vertical cross section through the 15 December 2006 break convection indicates deep convective cores of 40 dBZ reaching to 10 km with strong reflectivities (~ 55 dBZ) in the mid levels (Fig. 6). The 5-dBZ echo tops extend to 18 km. Application of the HID outlined in section 3 along this vertical cross section reveals bulk microphysics associated with the break convective core (Fig. 6). The upper regions of the storm are characterized by graupel, of both high and low density, as

well as regions of ice crystals and some vertical ice near the echo top. These categories indicate there could be charging mechanisms leading to lightning production, which is enhanced during the break periods relative to the monsoon (Rutledge et al. 1992; Williams et al. 1992; May et al. 2008). Regions of hail are concentrated at heights from 5 to 7 km, which then make a transition to large drops/melting hail between 3 and 5 km. Concentrations of hail at these heights are likely due to an active area of coalescence freezing and subsequent riming growth (Carey and Rutledge 2000). This is consistent with the Rasmussen and Heymsfield (1987a,b) melting model discussed previously; we would expect to see a peak in large drops around 1–2 km below the climatological melting layer (4.5–5.0 km) where the hailstones

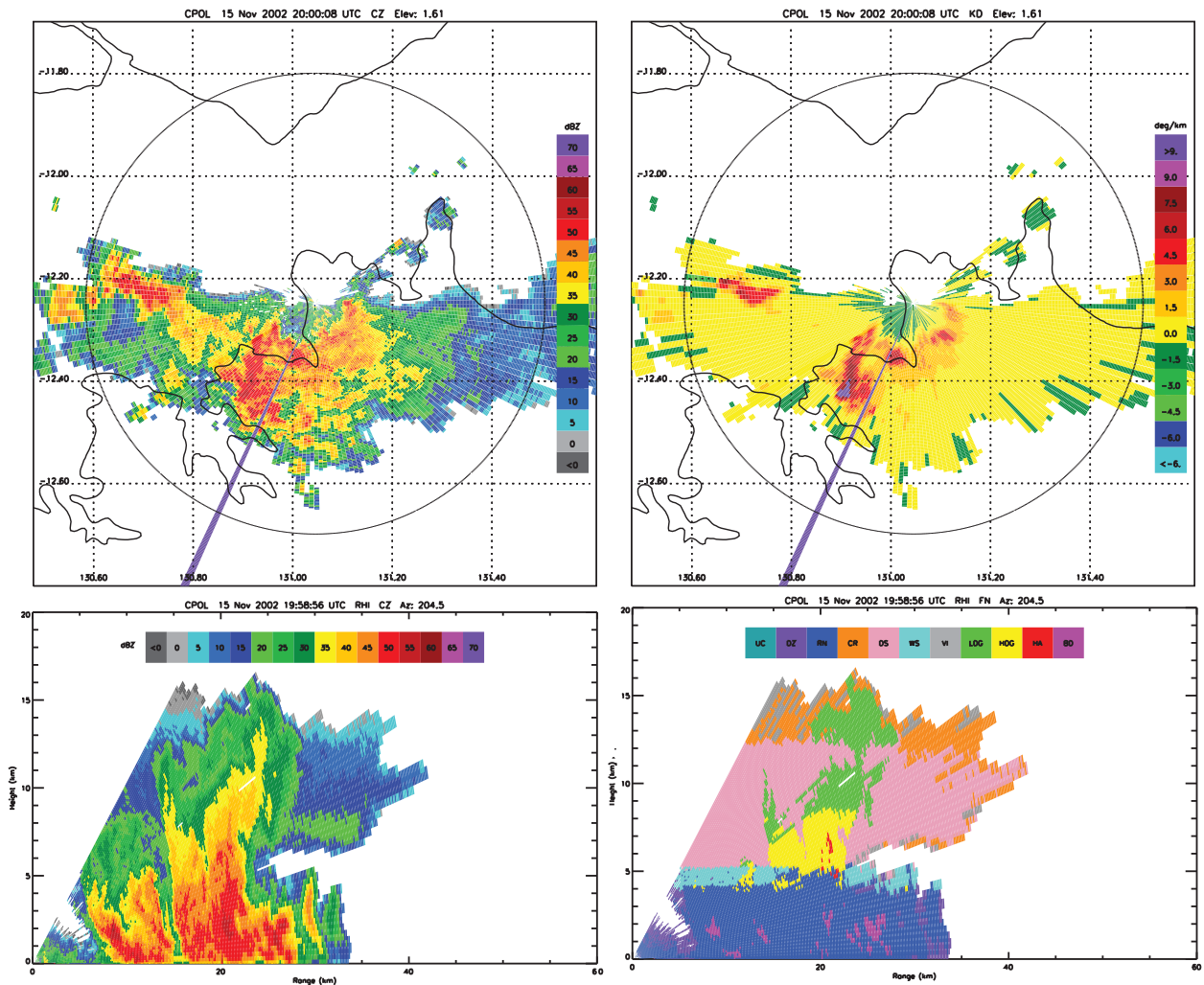


FIG. 7. Similar to Fig. 6, but showing an example of break convection from 2000 UTC 15 Nov 2002 and depicting (top right) the K_{dp} low-level PPI.

have had enough time to melt. Conversely, this category could indicate the presence of melting hail that has formed a torus of water and is falling relatively stably. Regions of dry aggregated snow encase the outer flanks of the convective core above the melting layer. These aggregates then make a transition to wet snow as they melt, and then they form rain and drizzle below.

A vertical cross section along a radial at 204.5° during the 15 November 2002 break case shows similar deep convective development (Fig. 7). Intense reflectivities greater than 50 dBZ extend up to 5 km, with some reaching even higher to 7 km, with a finger of greater than 35 dBZ up to nearly 15 km. The associated HID reveals some hail extending from above 5 km up to 7 km associated with the most intense convective core, with regions of big drops/melting hail below the melting layer. Large regions of low-density graupel stretch to

15 km, while areas of high-density graupel are apparent in the mixed-phase levels from 5 to 8 km and are presumably associated with vigorous updrafts. A small anvil of dry snow, ice crystals, and some vertical ice extends to the southwest.

In contrast to the break cross sections, a vertical RHI through the 15 March 2006 monsoon case reveals a large stratiform region with a small convective core with 40-dBZ reflectivities up to 6 km and 5-dBZ echo tops at 13–15 km (Fig. 8). The HID reveals a limited amount of high-density graupel in the main convective core, with a large region of dry aggregated snow melting into a distinct band of wet snow, with rain and drizzle below. Small regions of ice crystals are confined to the very top of the dry-aggregate region. No big drops or hail were identified. Of interest is that, although the melting layer is unmistakable in the HID as a band of wet snow,

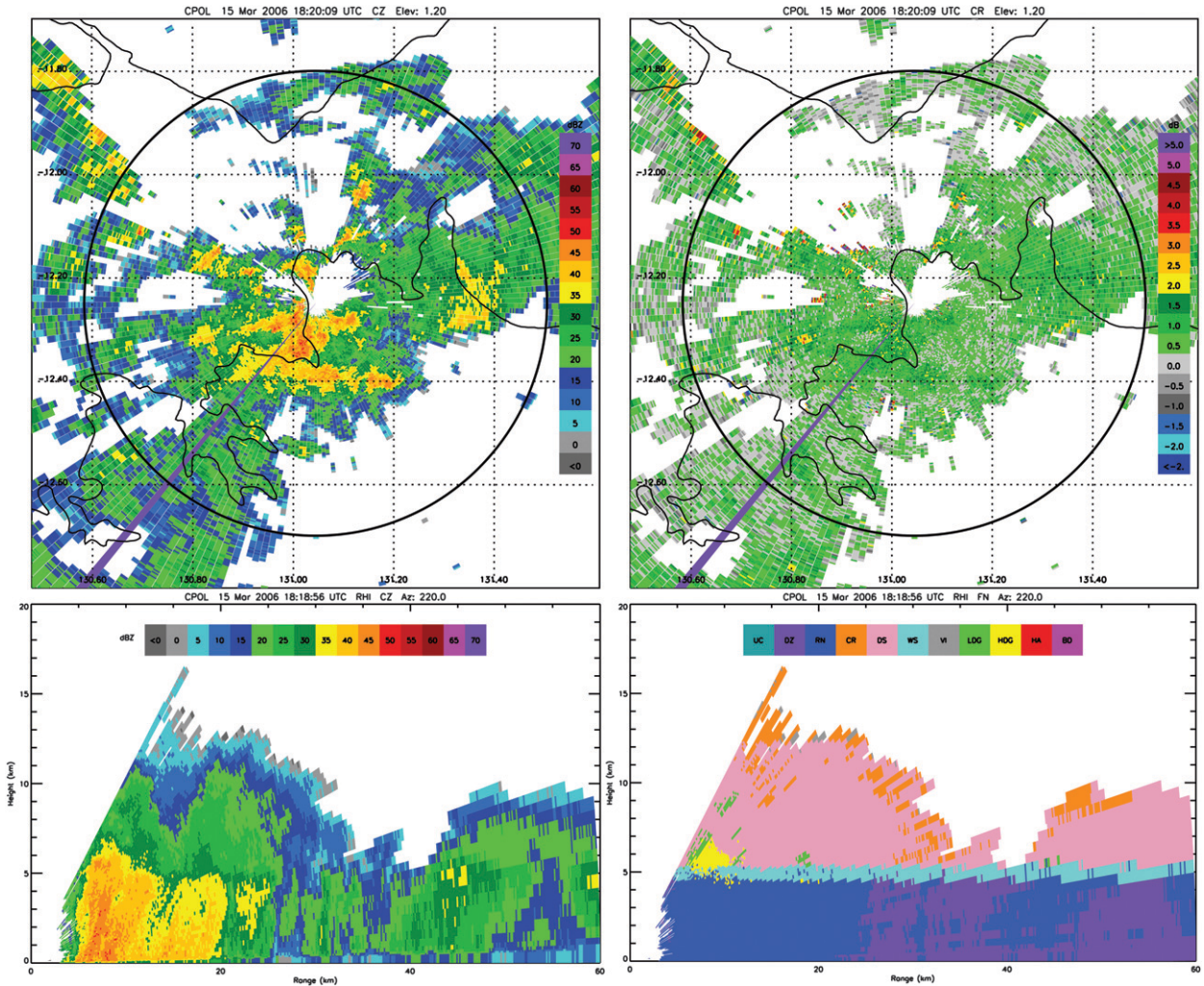


FIG. 8. Similar to Fig. 6, but showing an example of typical monsoon convection from 1820 UTC 15 Mar 2006 and the RHIs are along 220° azimuth (illustrated by purple ray in top panels).

a radar bright band is not clearly evident in the reflectivity field. This shows the advantage of using all of the polarimetric data in the HID where signatures of melting are sometimes more evident. These results are consistent with May and Ballinger (2007), who found that the monsoon convection had larger components of stratiform and generally lower echo-top heights relative to the break convection, and with May and Keenan (2005), who found very little hail in monsoon cases.

Vertical cross sections along a 204.5° radial during the 12 January 2003 monsoon case show that high reflectivity values (>55 dBZ) are confined to a small region right around 5 km (Fig. 9). Although the 5-dBZ echo-top height is nearly 17 km, reflectivities of greater than 35 dBZ extend only up to 12 km, as compared with 15 km in the break examples. Hydrometeor classification shows a narrow region of hail just above the

melting layer at 6 km that is associated with the highest reflectivities. Values of specific differential phase in this same region are greater than $9^{\circ} \text{ km}^{-1}$ (not shown). Large regions of high-density graupel are identified from just below the melting layer (~4 km) to as high as 9 km, with low-density graupel above those levels. Large areas of dry snow surround the convective cores while the area below the melting layer is predominantly rain with a few pixels of large drops/melting hail. Note that this is an example of an unusually intense monsoon case with such large reflectivities and deep regions of high- and low-density graupel in comparison with a more typical monsoon example such as the 15 March 2006 case.

Over the longer-term 7-yr record, normalized frequency by height of bulk hydrometeor types (Fig. 10) reveals features that are similar to those of the example

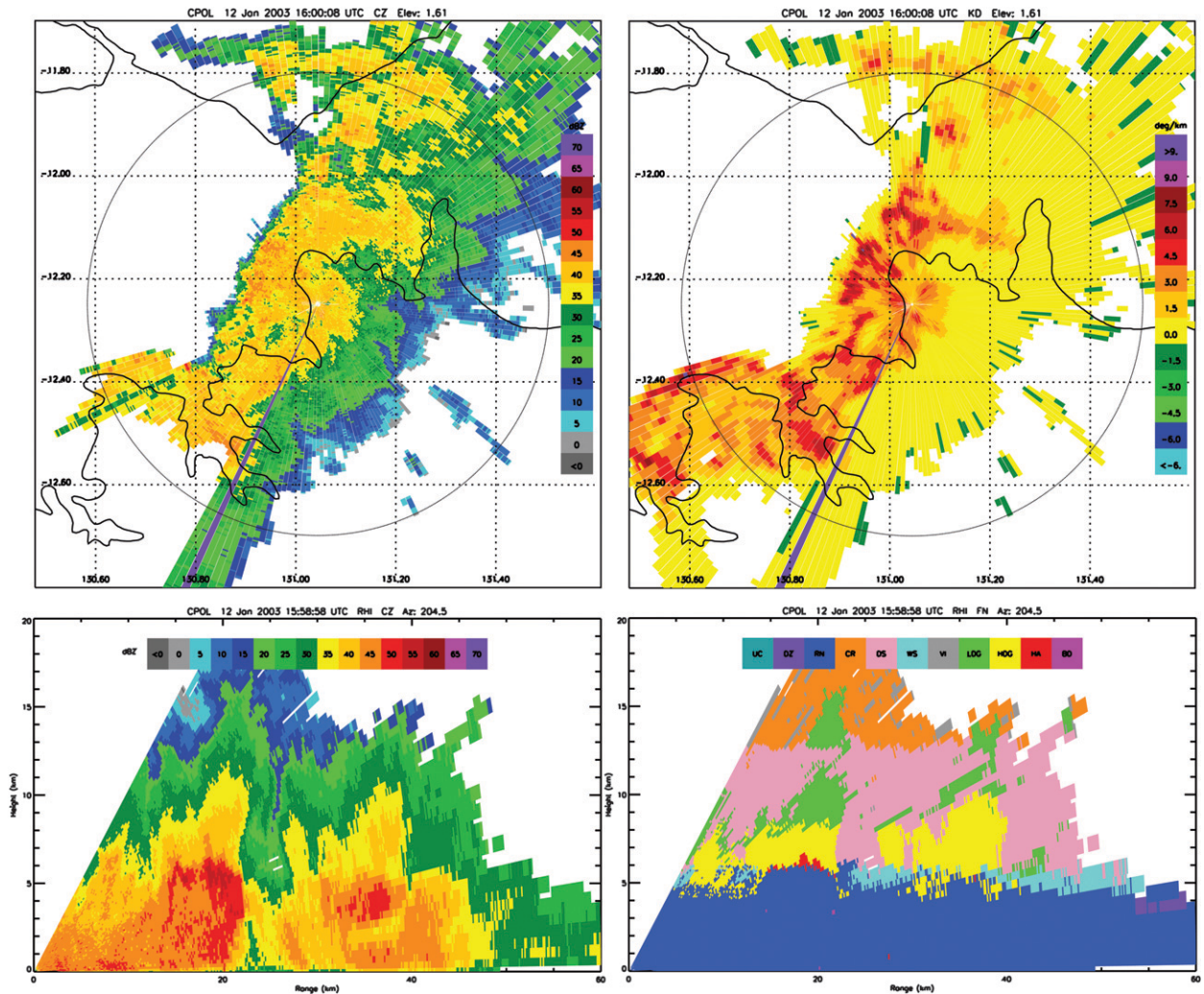


FIG. 9. As in Fig. 7, but showing an example of intense monsoon convection from 1600 UTC 12 Jan 2003.

monsoon and break cases. The break periods generally have more frequent vertically aligned ice in the very upper levels of the storms, which is indicative of strong electric fields in the anvils (Carey and Rutledge 1998; Ryzhkov et al. 1998; Ryzhkov and Zrnicek 1998; Straka et al. 2000), consistent with increased lightning activity during break periods (Rutledge et al. 1992; Williams et al. 1992). In addition, break periods have significantly more high-density graupel and more low-density graupel extending into the upper levels (9–16 km), whereas monsoon periods have larger frequencies of snow, low-density graupel, and ice crystals in the midlevels (5–9 km), as well as more wet snow, likely associated with bright bands in the extensive stratiform regions. Very little hail is identified at any height during the monsoon, whereas the break period has large amounts throughout the column with a peak frequency occurring at 6 km. Big

drops/melting hail are much more frequent during the break periods with a peak frequency at 3 km, about 3 km below the peak in hail and about 2 km below the average melting layer for Darwin. Big drops/melting hail also peak at 3 km during the monsoon but occur much less frequently.

During break (monsoon) periods, total convective fraction is 66% (37%) and stratiform fraction is 34% (63%). These percentages are consistent with May and Ballinger (2007), who found much higher stratiform fractions during the monsoon periods, and studies by Houze and Cheng (1977) that found that stratiform accounts for 40%–60% of precipitation in the tropics. The stratiform fraction is, however, much higher than that reported by Steiner and Houze (1997), who found that stratiform and convective precipitations were approximately equal during the monsoon in Darwin.

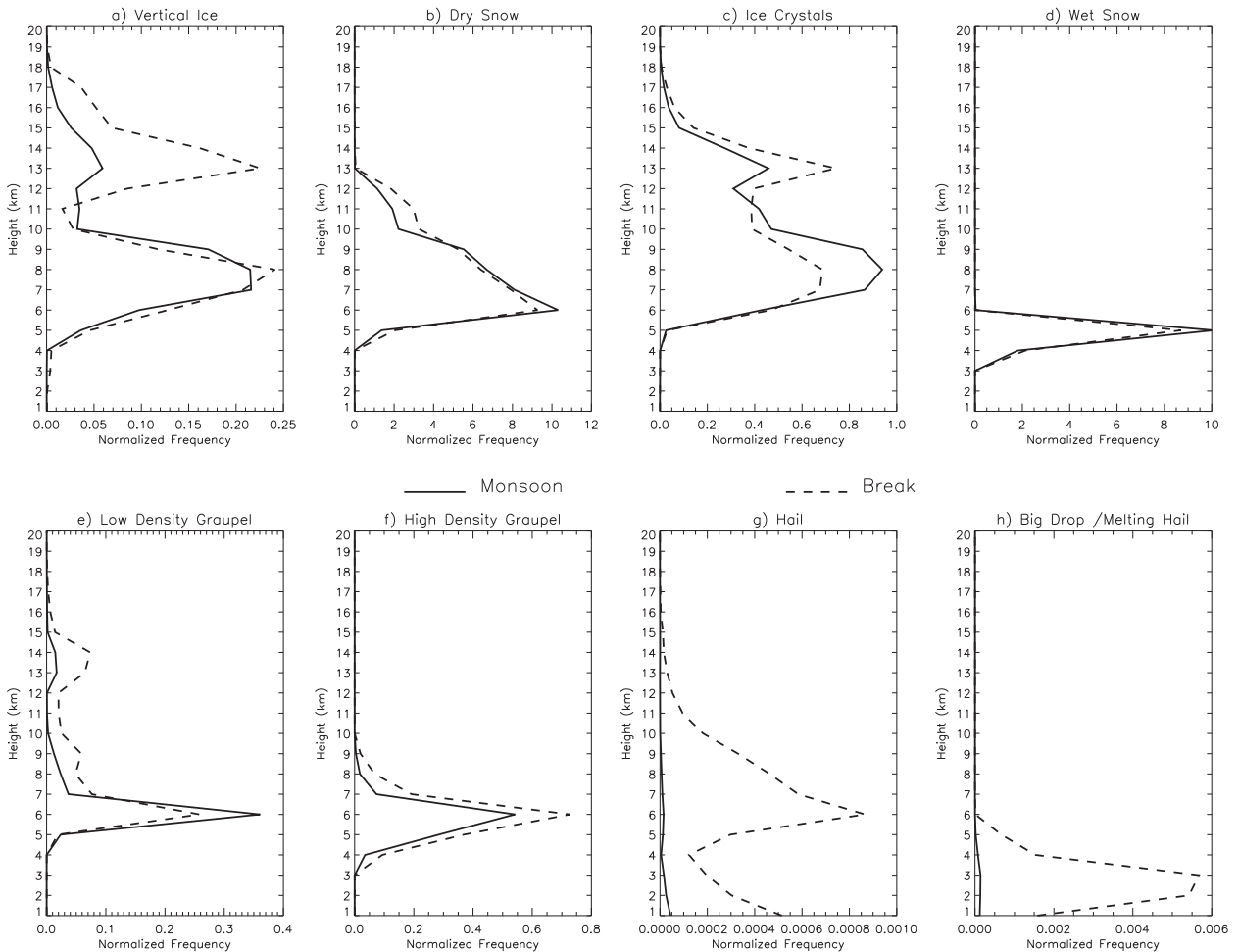


FIG. 10. Normalized frequency of hydrometeor types for break (dashed) and monsoon (solid) periods as a function of height for the entire seven seasons.

Profiles of mean stratiform reflectivities are similar between the two regimes (Fig. 11), with agreement at the surface and somewhat higher mean reflectivities during the break in the mid- and upper levels. Although these profiles lack a distinct peak at the 0°C isotherm associated with the radar bright band that has been noted in previous studies over Darwin (Cifelli and Rutledge 1998), this effect is likely smeared out by the grid resolution (2 km in the horizontal plane and 1 km in the vertical direction), and a distinct increase in reflectivity is obvious within 1 km of the climatological melting layer (4.5 km). The profiles are similar to past studies over Darwin in that reflectivity decreases toward the surface and in the upper levels, with maximum reflectivity in the midlevels, which is distinctly different from the convective profiles that have the highest mean reflectivities at or near the surface. The decrease in reflectivity below the bright band may be due to evaporation in the mesoscale downdraft in regions of stratiform

precipitation (Rasmussen and Rutledge 1993). In fact, this phenomenon is evident in mean profiles of differential reflectivity (Fig. 12), which increases slightly toward the surface consistent with the polarimetric characteristics of evaporation modeled by Kumjian and Ryzhkov (2010).

Mean convective reflectivity profiles (Fig. 11) illustrate key differences between convection during the two periods. Near the surface, convective profiles are within 1–2 dB, but near echo top these differences widen to nearly 6 dB. This is due to the vastly different shape of the profile, particularly through the mixed-phase region (4–8 km), where the monsoon profiles have steeper vertical gradients in reflectivity when compared with the break, leveling off in the upper levels at relatively weak values (20 dBZ), whereas break convection maintains higher reflectivities in the upper levels (25 dBZ). These observations are similar to previous studies of reflectivity profiles over the Darwin area (Williams et al. 1992;

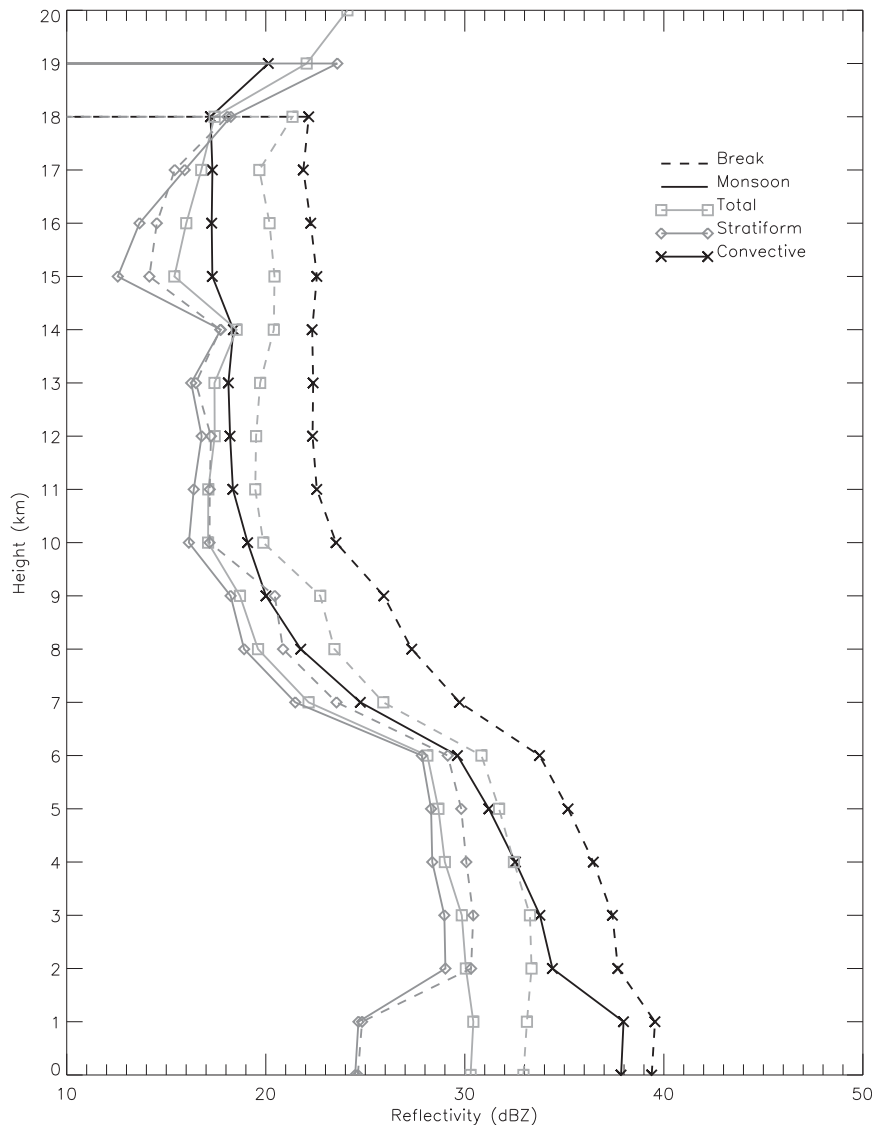


FIG. 11. Mean reflectivity profiles for convective (black lines with \times s), stratiform (medium-gray lines with diamonds), and total (light-gray lines with squares) elements for monsoon (solid lines) and break (dashed lines) periods over the entire seven seasons.

Zipser and Lutz 1994; Cifelli and Rutledge 1998) and other tropical regions (Cifelli et al. 2002) and are attributed to significantly fewer large particles above the melting layer (such as graupel and hail) and near-complete glaciation during oceanic-type conditions such as those associated with the monsoon (Rutledge et al. 1992; Williams et al. 1992; Zipser and Lutz 1994; Cifelli and Rutledge 1998). Below the melting layer, both convective profiles continue to increase toward the surface, with steeper gradients in the monsoon profile. Again, this has been observed in previous tropical studies (Zipser and Lutz 1994) and could be indicative of the prolific warm-rain processes that allow drops to grow in size

through coalescence as they fall in moisture-rich environments (Williams et al. 1992; Zipser and Lutz 1994; C00; C. Liu and E. Zipser 2011, personal communication) or through melting precipitation particles. Figure 13 illustrates how the frequency of mean convective drop diameters D_0 broadens toward the ground to include much larger mean drop diameters for both monsoon and break, which is also consistent with continued coalescence and/or melting hail acting to increase drop sizes.

Bringi et al. (2009) found that during the 2005/06 season mean convective and stratiform D_0 values were larger during break periods than for the monsoon and

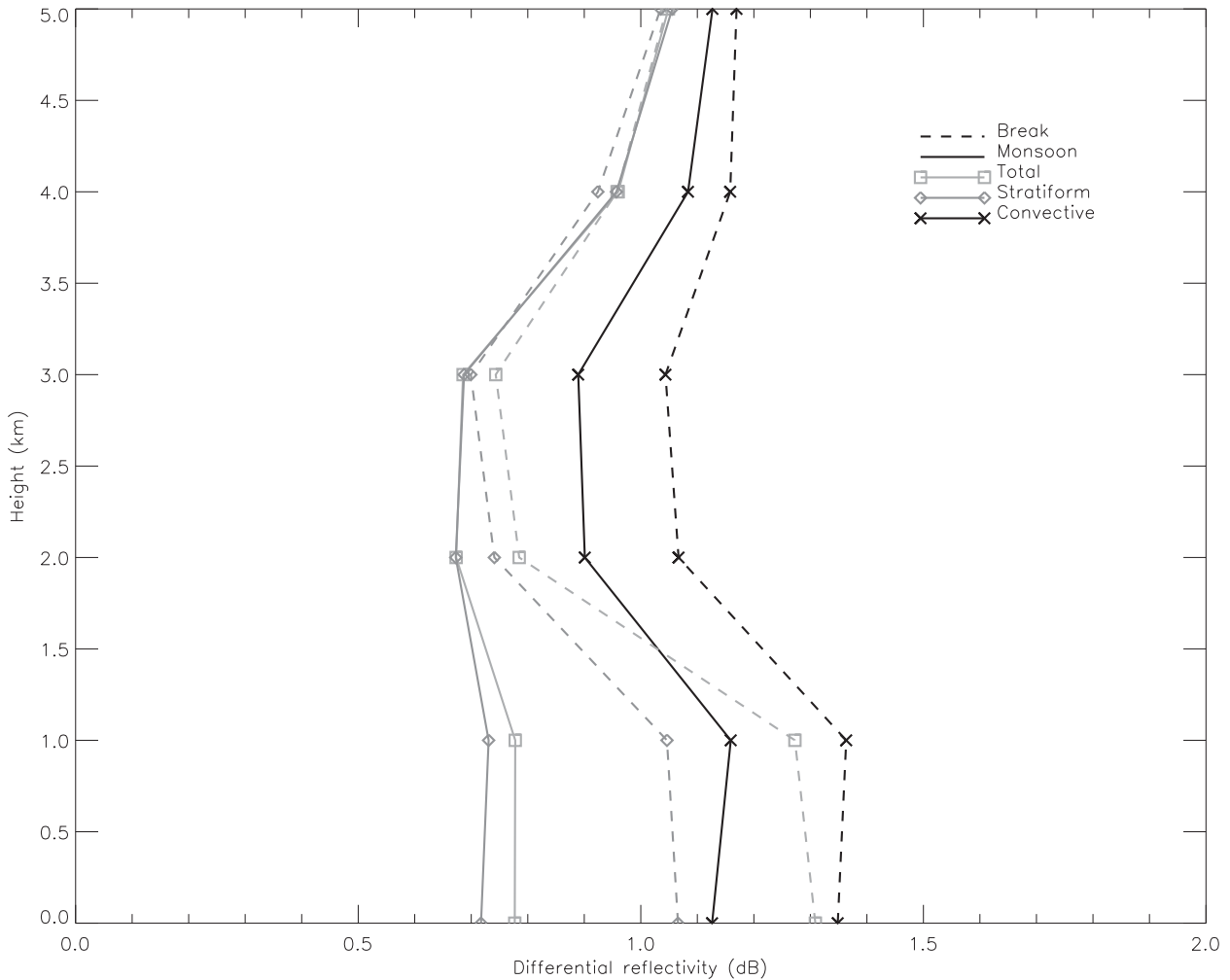


FIG. 12. Profile of mean Z_{dr} below 5 km, illustrating the slight increase between 2 km and the surface that is associated with evaporation. Convective (black lines with \times s), stratiform (medium-gray lines with diamonds), and total (light-gray lines with squares) elements for monsoon (solid lines) and break (dashed lines) periods are shown over the entire seven seasons.

additionally found that the distribution of D_0 values was broader during the break. These findings are also evident for the extended dataset (Fig. 13). Distributions of mean diameters D_0 are wider during the break periods than during the monsoon periods (Fig. 13) at all heights below the melting layer, indicating the presence of generally larger drops during break periods. This is especially pronounced in the convective components, where the most frequent mean diameter is larger during the break than during the monsoon below 3 km. Table 3 shows the most frequent D_0 at 1 km in height. The convective mean D_0 values are considerably different while the stratiform D_0 values are only slightly different. These results are similar to Bringi et al. (2009), who found during the TWP-ICE campaign that the break (monsoon) convective D_0 was 1.6 mm (1.44 mm), while the stratiform break (monsoon) D_0 was also larger at

1.34 mm (1.22 mm). Broader distributions of D_0 can indicate complicated rain formation processes such as coalescence or melting precipitation ice (Bringi et al. 2009). Of interest is that above 3 km the peak D_0 s are the same between the monsoon and break and for both convective and stratiform components, indicating large contributions of the sub-melting-layer environment to surface drop size distribution and precipitation characteristics.

Mean profiles of ice mass M_i (Fig. 14a) show that during the break periods precipitation ice extends to greater heights and has higher mixing in the convective cores when compared with the monsoon convection. This is likely an effect of the increased hail during break periods that dominates the ice mass in convective regions. In addition, both Rutledge et al. (1992) and Williams et al. (1992) found higher CAPE during the

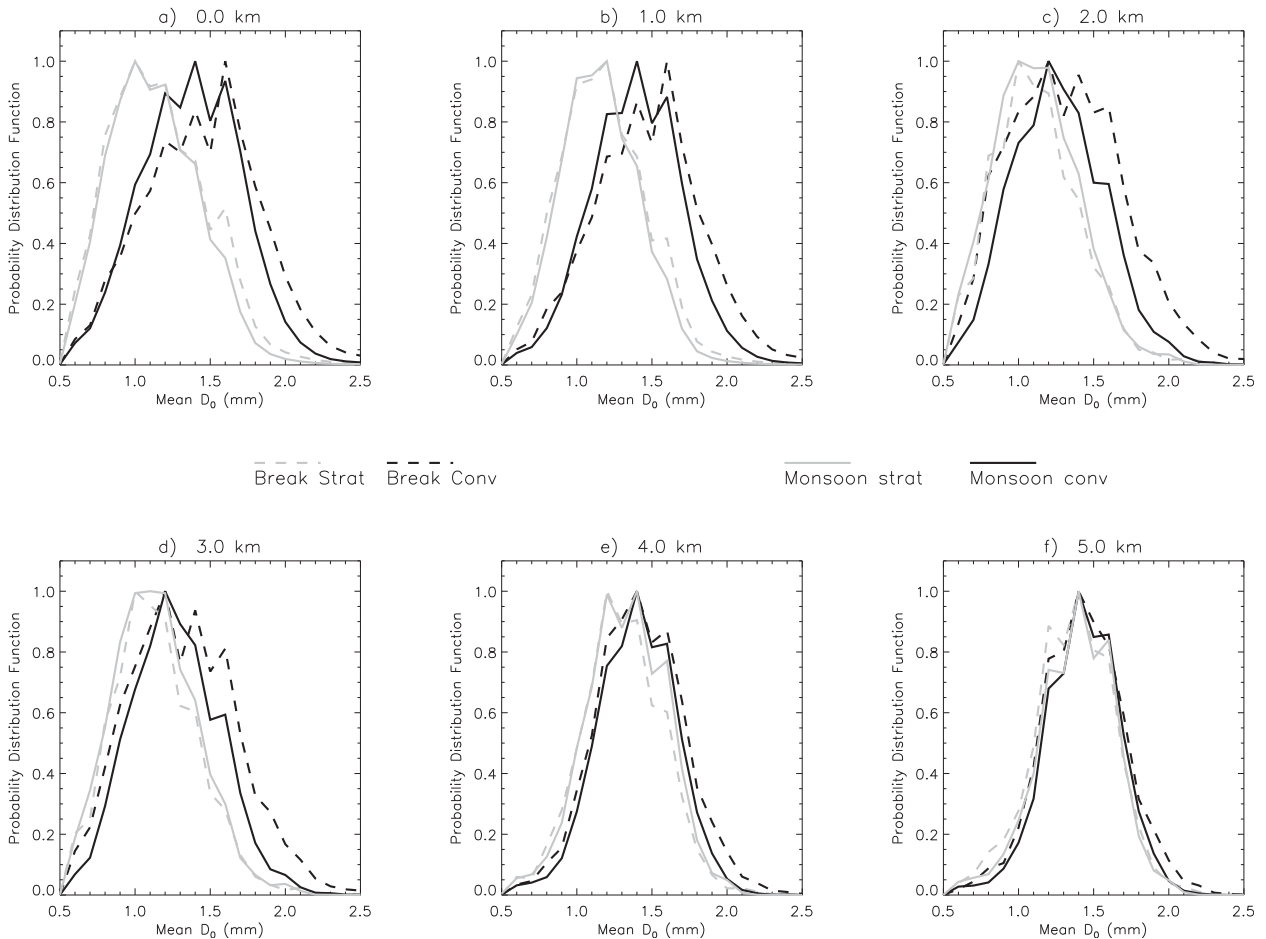


FIG. 13. Frequency distributions of convective (black curves) and stratiform (gray curves) D_0 as a function of height from 0.0 to 5.0 km for monsoon (solid curves) and break (dashed curves) periods during seven seasons of C-POL data.

break than during the monsoon, supporting larger vertical motions. The monsoon stratiform regions have peak mass contents just above the melting layer (6 km), whereas the break stratiform remains relatively low throughout the column. Water masses for rain have very similar profiles for convection during the break and monsoon, with the break having slightly higher liquid water mass (Fig. 14b). The stratiform liquid water concentrations are nearly identical during the two periods. Cumulative distribution frequencies of ice water path (IWP) and liquid water paths (LWP) are shown in Fig. 14c. Break periods are associated with more frequent higher IWPs when compared with the monsoon. The total convective IWP fraction during the monsoon is 2.0%, whereas during the break it is 3 times that, at 6.2%. This result suggests more mixed-phase precipitation physics relative to the warm-rain-dominated monsoon periods, during which smaller IWPs are frequent.

In general, the break periods have more frequent occurrences of heavy rain rates than do the monsoon periods (Fig. 15a). In terms of rain volume, however, more of the rain volume is contained in lighter rain rates during the monsoon (Fig. 15b). There is a notable difference between the break and monsoon rain volumes, where 78.5% (74.9%) of the rain volume is due to rain rates of 10 mm h^{-1} or less during monsoon (break) periods. This is consistent with other studies that have found the majority of the rain during the monsoon is

TABLE 3. Mean D_0 at 1-km height.

	Monsoon		Break	
	Mean D_0 (mm)	No. of points	Mean D_0 (mm)	No. of points
Convective	1.44	8.25×10^6	1.52	7.12×10^6
Stratiform	1.21	3.44×10^7	1.23	1.75×10^7

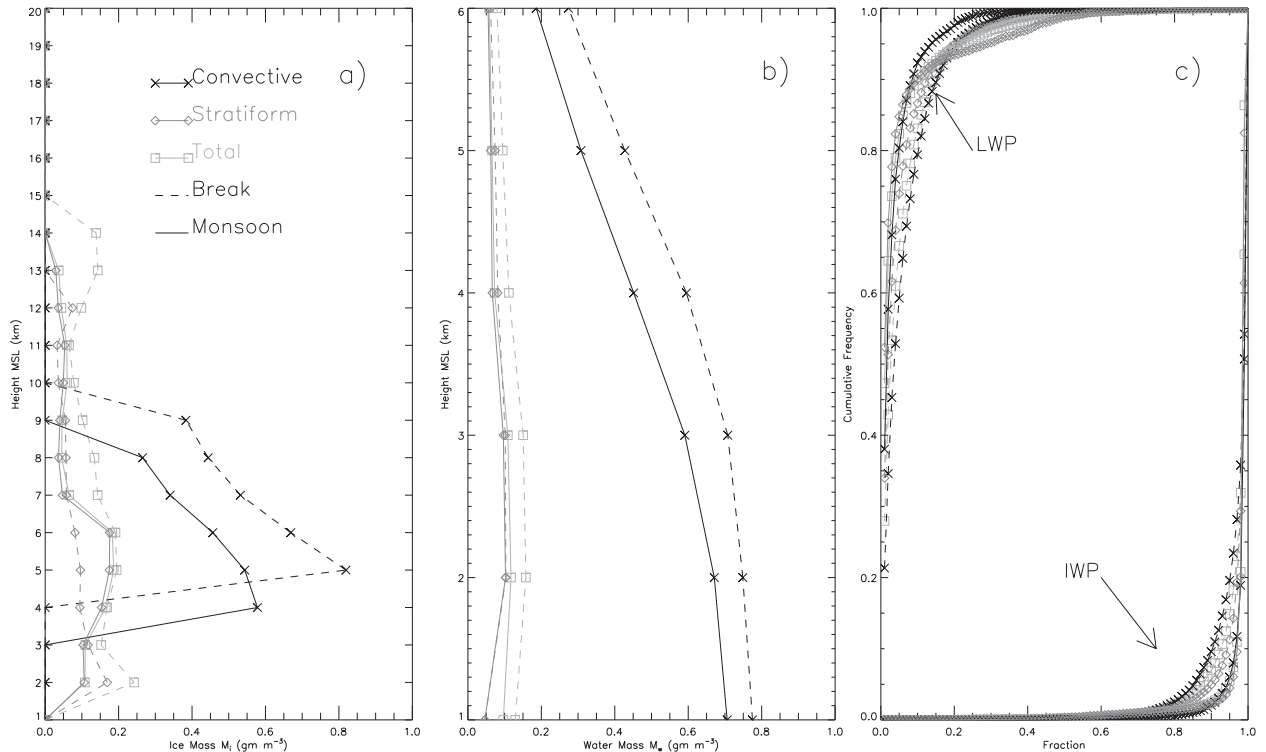


FIG. 14. (a) Precipitation ice mass M_i , (b) liquid water mass M_w , and (c) IWP (lower-right corner) and LWP (upper-left corner) fractions for convective (black curves with \times s), stratiform (medium-gray curves with diamonds), and total (light-gray curves with squares) elements for monsoon (solid curves) and break (dashed curves) periods for seven seasons of C-POL data. IWP and LWP fractions are defined as $\text{IWP}/(\text{LWP} + \text{IWP})$ and $\text{LWP}/(\text{LWP} + \text{IWP})$.

stratiform (Rutledge et al. 1992; May and Ballinger 2007). In terms of daily average accumulation over the entire grid domain ($100 \text{ km} \times 100 \text{ km}$), the mean accumulation during the monsoon is 43 mm, whereas during the break period it is less than one-half of that value, 18 mm. Thus, despite the frequent heavy rain rates during break periods, the short-lived, localized, and propagating nature of the break convection results in significantly less total accumulation in comparison with the monsoon. Break periods tend to have increased frequency of high rain rates relative to monsoon periods for both stratiform and convective components (Fig. 15a). During the monsoon, however, the lighter rain rates contribute more to the overall rain volume than they do during break periods (Fig. 15c), which is consistent with the monsoon providing significantly more rainfall to the area through large stratiform shields (Rutledge et al. 1992; May and Ballinger 2007).

5. Conclusions

Despite some significant challenges caused by attenuation, Mie scattering, and resonance effects, a C-band hydrometeor identification algorithm was developed

and applied to seven seasons of C-POL observations to investigate microphysical differences between precipitation occurring under two distinct meteorological regimes. Although Mie effects may preclude confidently distinguishing melting hail from rain under certain circumstances, significant Mie effects in large, wetted particles provide a relatively reliable means to identify wet snow. The new theoretical HID produces realistic microphysical continuity, providing some indirect validation of the algorithm, with hail in the midlevels, wet snow around the melting level, and big drops/melting hail below regions where large-precipitation ice is likely melting or melted.

Application of the HID to seven seasons of polarimetric observations from C-POL radar in Darwin revealed significant differences in the microphysical structure of convection occurring during the break and monsoon periods. Hail, big drops/melting hail, and vertical ice occur considerably more frequently during the break than during the monsoon. This is likely due to the more intense, vertically developed nature of break convection, which is able to produce updraft speeds that are conducive to hail growth. These large hail stones then fall through the warm, moist environment and melt to become large, relatively

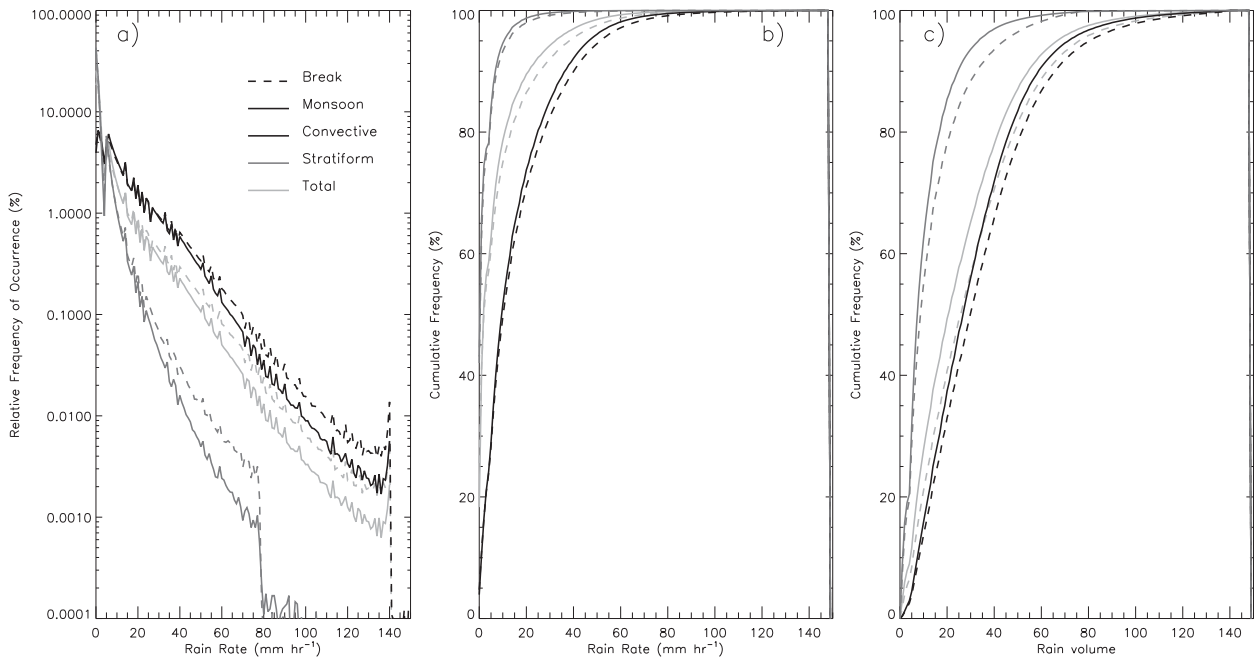


FIG. 15. (a) Relative frequency of rain rates, (b) cumulative frequency distribution of rain rates, and (c) cumulative frequency distribution of rain volume for convective (black curves), stratiform (medium-gray curves), and total (light-gray curves) volumes for monsoon (solid curves) and break (dashed curves) periods during seven seasons of C-POL data.

flat water targets. Significant vertical ice at heights above 10 km during the break periods suggests strong electric fields that align small ice crystals along their major axis. On the other hand, low-density graupel and wet and dry snow occur more frequently around the melting layer during the monsoon. This is a result of the less intense, more stratiform nature of monsoon convection whereby large aggregates melt to produce a definite brightband signature. The large amount of graupel indicates that some amount of riming is associated with the monsoon but not enough to produce widespread hail.

Reflectivity profiles suggested that prolific coalescence and/or precipitation ice-melting processes occur in the convective partitions of both monsoon and break

convection, with increasing reflectivities below the melting layer. Frequency distributions of mean drop diameters D_0 supported this finding with spectra broadening to include larger mean diameters toward the surface. In contrast, reflectivity profiles of stratiform regions show decreasing reflectivities below the melting layer, with coincident narrowing of D_0 histograms and increases in differential reflectivities near the surface, suggesting evaporation processes. We speculate that this may be due to evaporation in large stratiform regions of squall lines associated with mesoscale downdrafts.

Break periods had greater precipitation ice mixing ratios to higher heights and larger convective IWP fractions, suggesting more mixed-phase precipitation

TABLE A1. Simulated polarimetric variable ranges for hydrometeors at C band (5.5 cm) and associated temperature ranges ($^{\circ}\text{C}$).

	Z_h		Z_{dr}		K_{dp}		ρ_{hv}		Temperature
	Min	Max	Min	Max	Min	Max	Min	Max	
Drizzle	-27.3	30.8	0.0	0.9	0.0	0.1	0.982	1.018	> -1.0
Rain	20.0	58.0	0.1	4.5	0.0	11.0	0.975	1.025	> -3.0
Ice crystals	-24.9	19.3	0.2	5.6	0.0	0.2	0.955	1.005	< 0.0
Aggregates	-1.1	35.1	-0.1	2.1	-0.3	0.3	0.86	1.00	$-51.0 < T < 1.0$
Wet snow	2.7	45.3	0.40	2.2	-0.2	0.7	0.49	0.99	$-2.5 < T < 4.5$
High-density graupel	34.1	54.5	0.40	2.8	0.0	3.8	0.96	1.04	$-22.5 < T < 17.5$
Low-density graupel	27.8	46.2	0.0	1.8	0.0	0.2	0.975	1.025	< 0.0
Hail	48.0	76.6	-0.4	0.7	-2.9	4.1	0.87	1.07	—
Big drops	49.3	66.3	2.5	6.3	0.1	6.7	0.96	1.02	> -3.0
Vertical aligned ice	-26.0	24.0	-1.8	0.0	-1.5	0.0	0.953	0.996	< 0.0

TABLE A2. Membership beta function parameters for C-band (5.5 cm) HID, where a is half-width, m is the center, and b is the slope of the beta functions.

	Z_h			Z_{dr}			K_{dp}			ρ_{hv}			Temperature		
	m	a	b	m	a	b	m	a	b	m	a	b	m	a	b
Drizzle	1.75	29	10.0	0.46	0.46	5.0	0.03	0.03	2.0	1.0	0.018	3.0	40.0	41.0	50.0
Rain	39	19	10.0	2.3	2.2	9.0	5.5	5.5	10.0	1.0	0.025	3.0	48.0	51.0	30.0
Ice crystals	-2.8	22.1	20.0	2.9	2.7	10.0	0.08	0.08	6.0	0.98	0.025	3.0	-50.0	50.0	25.0
Aggregates	17.0	18.1	10.0	1.0	1.1	7.0	-0.008	0.3	1.0	0.93	0.07	3.0	-25.0	26.0	15.0
Wet snow	24.0	21.3	10.0	1.3	0.9	10.0	0.25	0.43	6.0	0.74	0.25	10.0	1.0	3.5	5.0
High-density graupel	44.3	10.2	6.0	1.6	1.2	3.0	1.9	1.9	3.0	1.0	0.04	2.0	-2.5	20.0	2.0
Low-density graupel	37.0	9.2	0.8	0.9	0.9	6.0	0.1	0.08	3.0	1.0	0.025	1.0	-50.0	50.0	25.0
Hail	62.3	14.3	10.0	0.14	0.56	8.0	0.6	3.5	6.0	0.97	0.1	3.0	0.0	100.0	5.0
Big drops	57.8	8.5	10.0	4.4	1.9	8.0	3.4	3.3	6.0	0.99	0.03	3.0	48.0	21.0	30.0
Vertical aligned ice	-1.0	25.0	20.0	-0.90	0.9	10.0	-0.75	0.75	30.0	0.975	0.022	3.0	-50.0	50.0	25.0

generation, as compared with more warm-rain processes during the monsoon. In fact, the majority of the rainfall during the monsoon is due to stratiform components (63%), as compared with the break (34%). This is also evidenced by the frequencies of D_0 . Both stratiform and convective D_0 values are slightly larger during break periods than during the monsoon. More important, the distribution of D_0 is wider and includes occurrences of much larger values during the break. This indicates that rain drops may be forming because of melting ice particles such as graupel or hail.

Higher convective and stratiform rain rates occur more frequently during the break than during the monsoon. During the monsoon, however, lighter rain rates contribute more to the overall rain volume. Despite the lighter rain rates, the widespread stratiform regions associated with monsoon convection produce much-larger average daily rainfall accumulations in comparison with break periods.

Acknowledgments. The authors thank Dr. Peter May at the Australian Bureau of Meteorology and David B. Wolff at NASA Wallops Flight Facility for providing the C-POL data; Dr. Christopher Williams (Cooperative Institute for Research in Environmental Sciences, University of Colorado) supplied the JWD and tipping-bucket data for rainfall comparisons. Doctors Timothy Lang and Angela Rowe (Colorado State University) contributed through insightful discussions. Paul Hein (Colorado State University) provided significant assistance with the data processing. The NASA TRMM validation office provided software for radar visualization. The authors are grateful to three anonymous reviewers who offered valuable comments for improving the manuscript. This research is funded primarily by

NASA Precipitation Measurement Mission Grants NNX10AG88 and NNX10AG82G and NASA Ground Validation Grant NNX11AD03G.

APPENDIX

C-Band Hydrometeor Ranges

Simulated polarimetric variable ranges for hydrometeors at C band (5.5 cm), and associated temperature ranges, that were used to define the membership beta functions are given in Table A1. The associated membership beta function parameters for the C-band HID are presented in Table A2.

REFERENCES

Alberoni, P. P., D. Zrnicek, A. Ryzhkov, and L. Guerrieri, 2002: Use of a fuzzy logic classification scheme with a C-band polarimetric radar: First results. *Proc. European Radar Conf.*, Delft, Netherlands, ERAD, 324–327.

Anderson, M. E., L. D. Carey, W. A. Petersen, and K. R. Knupp, 2011: C-band dual-polarimetric radar signatures of hail. *Electron. J. Oper. Meteor.*, **2011-EJ2**. [Available online at <http://www.nwas.org/ej/pdf/2011-EJ2.pdf>.]

Baldini, L., E. Gorgucci, V. Chandrasekar, and W. Petersen, 2005: Implementations of CSU hydrometeor classification scheme for C-band polarimetric radars. Preprints, *32nd Conf. on Radar Meteorology*, Albuquerque, NM, Amer. Meteor. Soc., P11R.4. [Available online at <https://ams.confex.com/ams/pdfpapers/95865.pdf>.]

Battan, L. J., 1979: *Radar Observation of the Atmosphere*. University of Chicago Press, 324 pp.

Bringi, V. N., V. Chandrasekar, N. Balakrishnan, and D. S. Zrnicek, 1990: An examination of propagation effects in rainfall on radar measurements at microwave frequencies. *J. Atmos. Oceanic Technol.*, **7**, 829–840.

- , —, P. Meischner, J. Hubbert, and Y. Golestani, 1991: Polarimetric radar signatures of precipitation at S and C bands. *IEEE Proc.*, **138**, 109–119.
- , M. Thurai, K. Nakagawa, G. J. Huang, T. Kobayashi, A. Adachi, H. Hanado, and S. Sekizawa, 2006: Rainfall estimation from C-band polarimetric radar in Okinawa, Japan: Comparisons with 2D-video disdrometer and 400 MHz wind profiler. *J. Meteor. Soc. Japan*, **84**, 705–724.
- , C. R. Williams, M. Thurai, and P. T. May, 2009: Using dual-polarized radar and dual-frequency profiler for DSD characterization: A case study from Darwin, Australia. *J. Atmos. Oceanic Technol.*, **26**, 2107–2122.
- Carey, L. D., and S. A. Rutledge, 1998: Electrical and multiparameter radar observations of a severe hailstorm. *J. Geophys. Res.*, **103**, 13 979–14 000.
- , and —, 2000: The relationship between precipitation and lightning in tropical island convection: A C-band polarimetric radar study. *Mon. Wea. Rev.*, **128**, 2687–2710.
- , —, D. A. Ahijevych, and T. D. Keenan, 2000: Correcting propagation effects in C-Band polarimetric radar observations of tropical convection using differential propagation phase. *J. Appl. Meteor.*, **39**, 1405–1433.
- , W. A. Petersen, and W. K. Deierling, 2009: Radar differential phase signatures of ice orientation for the prediction of lightning initiation and cessation. Preprints, *34th Conf. on Radar Meteorology*, Williamsburg, VA, Amer. Meteor. Soc., 10A.2. [Available online at <https://ams.confex.com/ams/pdfpapers/155707.pdf>.]
- Chandrasekar, V., R. Keränen, S. Lim, and D. Moiseev, 2013: Recent advances in classification of observations from dual polarization weather radars. *Atmos. Res.*, **119**, 97–111.
- Cheng, L., and M. English, 1983: A relationship between hailstone concentration and size. *J. Atmos. Sci.*, **40**, 204–213.
- Cifelli, R., and S. A. Rutledge, 1998: Vertical motion, diabatic heating, and rainfall characteristics in north Australia convective systems. *Quart. J. Roy. Meteor. Soc.*, **124**, 1133–1162.
- , W. A. Petersen, L. D. Carey, S. A. Rutledge, and M. A. F. da Silva Dias, 2002: Radar observations of the kinematic, microphysical, and precipitation characteristics of two MCSs in TRMM LBA. *J. Geophys. Res.*, **107**, 8077, doi:10.1029/2000JD000264.
- , V. Chandrasekar, S. Lim, P. C. Kennedy, Y. Wang, and S. A. Rutledge, 2011: A new dual-polarization radar rainfall algorithm: Application in Colorado precipitation events. *J. Atmos. Oceanic Technol.*, **28**, 352–364.
- Depue, T. K., P. C. Kennedy, and S. A. Rutledge, 2007: Performance of the hail differential reflectivity (HDR) polarimetric radar hail indicator. *J. Appl. Meteor. Climatol.*, **46**, 1290–1301.
- Dolan, B., and S. A. Rutledge, 2009: A theory-based hydrometeor identification algorithm for X-band polarimetric radars. *J. Atmos. Oceanic Technol.*, **26**, 2071–2088.
- Drosowsky, W., 1996: Variability of the Australian summer monsoon at Darwin: 1957–1992. *J. Climate*, **9**, 85–96.
- Fabry, F., and W. Szyrmer, 1999: Modeling of the melting layer. Part II: Electromagnetic. *J. Atmos. Sci.*, **56**, 3593–3600.
- Goddard, J. W. F., J. D. Eastment, and J. Tan, 1994: Self-consistent measurements of differential phase and differential reflectivity in rain. *Proc. Int. Geoscience Remote Sensing Symp.*, Pasadena, CA, IEEE, 369–371.
- Gorgucci, E., G. Scarchilli, and V. Chandrasekar, 1992: Calibration of radars using polarimetric techniques. *IEEE Trans. Remote Sens.*, **30**, 853–858.
- , —, and —, 1999: A procedure to calibrate multiparameter weather radar using properties of the rain medium. *IEEE Trans. Remote Sens.*, **37**, 269–276.
- , V. Chandrasekar, and L. Baldini, 2006: Correction of X-band radar observation for propagation effects based on the self-consistency principle. *J. Atmos. Oceanic Technol.*, **23**, 1668–1681.
- Gunn, K. L. S., and J. S. Marshall, 1958: The distribution with size of aggregate snowflakes. *J. Meteor.*, **15**, 452–461.
- Hendon, H. H., and B. Liebmann, 1990: A composite study of onset of the Australian summer monsoon. *J. Atmos. Sci.*, **47**, 2227–2240.
- Holland, G. J., 1986: Interannual variability of the Australian summer monsoon at Darwin: 1952–82. *Mon. Wea. Rev.*, **114**, 594–604.
- Houze, R. A., Jr., and C.-P. Cheng, 1977: Radar characteristics of tropical convection observed during GATE: Mean properties and trends over the summer season. *Mon. Wea. Rev.*, **105**, 964–980.
- Kaltenboeck, R., and A. Ryzhkov, 2013: Comparison of polarimetric signatures of hail at S and C bands for different hail sizes. *Atmos. Res.*, **123**, 323–336.
- Keenan, T., 2003: Hydrometeor classification with a C-band polarimetric radar. *Aust. Meteor. Mag.*, **52**, 23–31.
- , and R. E. Carbone, 1992: A preliminary morphology of precipitation systems in tropical northern Australia. *Quart. J. Roy. Meteor. Soc.*, **118**, 283–326.
- , and S. A. Rutledge, 1993: Mesoscale characteristics of monsoonal convection and associated stratiform precipitation. *Mon. Wea. Rev.*, **121**, 352–374.
- , K. Glasson, F. Cummings, T. S. Bird, J. Keeler, and J. Lutz, 1998: The BMRC/NCAR C-band polarimetric (C-POL) radar system. *J. Atmos. Oceanic Technol.*, **15**, 871–886.
- , L. D. Carey, D. S. Zrnic, and P. T. May, 2001: Sensitivity of 5-cm wavelength polarimetric radar variables to raindrop axial ratio and drop size distribution. *J. Appl. Meteor.*, **40**, 524–545.
- Keranen, R., E. Saltikoff, V. Chandrasekar, S. Lim, J. Holmes, and J. Selzler, 2007: Real-time hydrometeor classification for the operational forecasting environment. Preprints, *33rd Conf. on Radar Meteorology*, Cairns, Australia, Amer. Meteor. Soc., P11B.11. [Available online at <https://ams.confex.com/ams/pdfpapers/123476.pdf>.]
- Knight, C. A., and N. C. Knight, 1970: The falling behavior of hailstones. *J. Atmos. Sci.*, **27**, 672–680.
- Knight, N. C., 1986: Hailstone shape factor and its relation to radar interpretation of hail. *J. Climate Appl. Meteor.*, **25**, 1956–1958.
- Kumjian, M. R., and A. V. Ryzhkov, 2008: Polarimetric signatures in supercell thunderstorms. *J. Appl. Meteor. Climatol.*, **47**, 1940–1961.
- , and —, 2010: The impact of evaporation on polarimetric characteristics of rain: Theoretical model and practical implications. *J. Appl. Meteor. Climatol.*, **49**, 1247–1267.
- Lang, T. J., S. A. Rutledge, and R. Cifelli, 2010: Polarimetric radar observations of convection in northwestern Mexico during the North American Monsoon Experiment. *J. Hydrometeorol.*, **11**, 1345–1357.
- Lim, S., V. Chandrasekar, and V. N. Bringi, 2005: Hydrometeor classification system using dual-polarization radar measurements: Model improvements and in situ verification. *IEEE Trans. Geosci. Remote Sens.*, **43**, 792–801.
- List, R., U. W. Rentsch, A. C. Byram, and E. P. Lozowski, 1973: On the aerodynamics of spheroidal hailstone models. *J. Atmos. Sci.*, **30**, 653–661.

- Liu, H., and V. Chandrasekar, 2000: Classification of hydrometeors based on polarimetric radar measurements: Development of fuzzy logic and neuro-fuzzy systems, and in situ verification. *J. Atmos. Oceanic Technol.*, **17**, 140–164.
- Mapes, B., and R. A. Houze Jr., 1992: An integrated view of the 1987 Australian monsoon and its mesoscale convective systems. Part 1: Horizontal structure. *Quart. J. Roy. Meteor. Soc.*, **118**, 927–963.
- Marzano, F. S., D. Scaranari, P. P. Alberoni, G. Vulpiani, and M. Montopoli, 2006: Hydrometeor classification from dual-polarized weather radar: extending fuzzy logic from S-band to C-band data. *Adv. Geosci.*, **7**, 109–114.
- , —, and G. Vulpiani, 2007: Supervised fuzzy-logic classification of hydrometeors using C-band weather radars. *IEEE Trans. Geosci. Remote Sens.*, **45**, 3784–3799.
- May, P. T., and T. D. Keenan, 2005: Evaluation of microphysical retrievals from polarimetric radar with wind profiler data. *J. Appl. Meteor.*, **44**, 827–838.
- , and A. Ballinger, 2007: The statistical characteristics of convective cells in a monsoon regime (Darwin, Northern Australia). *Mon. Wea. Rev.*, **135**, 82–92.
- , A. R. Jameson, T. D. Keenan, and P. E. Johnston, 2001: A comparison between polarimetric radar and wind profiler observations of precipitation in tropical showers. *J. Appl. Meteor.*, **40**, 1702–1717.
- , —, —, —, and C. Lucas, 2002: Combined wind profiler/polarimetric radar studies of the vertical motion and microphysical characteristics of tropical sea breeze thunderstorms. *Mon. Wea. Rev.*, **130**, 2228–2239.
- , J. H. Mather, G. Vaughan, K. N. Bower, C. Jakob, G. M. McFarquhar, and G. G. Mace, 2008: The Tropical Warm Pool International Cloud Experiment. *Bull. Amer. Meteor. Soc.*, **89**, 629–645.
- Meischner, P. F., V. N. Bringi, D. Heimann, and H. Höller, 1991: A squall line in southern Germany: Kinematics and precipitation formation as deduced by advanced polarimetric and Doppler radar measurements. *Mon. Wea. Rev.*, **119**, 678–701.
- Park, H. S., A. V. Ryzhkov, D. S. Zrnica, and K.-E. Kim, 2009: The hydrometeor classification algorithm for the polarimetric WSR-88D: Description and application to an MCS. *Wea. Forecasting*, **24**, 730–748.
- Petersen, W. A., 1997: Multi-scale process studies in the tropics: Results from lightning observations. Ph.D. dissertation, Colorado State University, 354 pp.
- Picca, J., and A. Ryzhkov, 2012: A dual-wavelength polarimetric analysis of the 16 May 2010 Oklahoma City extreme hailstorm. *Mon. Wea. Rev.*, **140**, 1385–1403.
- Rasmussen, E. N., and S. A. Rutledge, 1993: Evolution of quasi-two-dimensional squall lines. Part I: Kinematic and reflectivity structure. *J. Atmos. Sci.*, **50**, 2584–2606.
- Rasmussen, R. M., and A. J. Heymsfield, 1987a: Melting and shedding of graupel and hail. Part I: Model physics. *J. Atmos. Sci.*, **44**, 2754–2763.
- , and —, 1987b: Melting and shedding of graupel and hail. Part II: Sensitivity study. *J. Atmos. Sci.*, **44**, 2764–2782.
- Russchenberg, H. W. J., and L. P. Ligthart, 1996: Backscattering by and propagation through the melting layer of precipitation: A new polarimetric model. *IEEE Trans. Remote Sens.*, **34**, 3–14.
- Rutledge, S. A., E. R. Williams, and T. D. Keenan, 1992: The Down Upper Doppler and Electricity Experiment (DUNDEE): Overview and preliminary results. *Bull. Amer. Meteor. Soc.*, **73**, 3–16.
- Ryzhkov, A. V., and D. S. Zrnica, 1995: Precipitation and attenuation measurements at a 10-cm wavelength. *J. Appl. Meteor.*, **34**, 2121–2134.
- , and —, 1998: Discrimination between rain and snow with a polarimetric radar. *J. Appl. Meteor.*, **37**, 1228–1240.
- , —, and B. A. Gordon, 1998: Polarimetric method for ice water content determination. *J. Appl. Meteor.*, **37**, 125–134.
- , S. E. Giangrande, V. M. Melnikov, and T. J. Schuur, 2005a: Calibration issues of dual-polarization radar measurements. *J. Atmos. Oceanic Technol.*, **22**, 1138–1155.
- , —, and T. J. Schuur, 2005b: Rainfall estimation with a polarimetric prototype of WSR-88D. *J. Appl. Meteor.*, **44**, 502–515.
- , T. J. Schuur, D. W. Burgess, P. L. Heinselman, S. E. Giangrande, and D. S. Zrnica, 2005c: The Joint Polarization Experiment. *Bull. Amer. Meteor. Soc.*, **86**, 809–824.
- , and Coauthors, 2007: Comparison of polarimetric algorithms for hydrometeor classification at S and C bands. Preprints, *33rd Conf. on Radar Meteorology*, Cairns, Australia, Amer. Meteor. Soc., 10.3. [Available online at <http://ams.confex.com/ams/pdfpapers/123109.pdf>.]
- , S. Ganson, A. Khain, M. Pinsky, and A. Pokrovsky, 2009: Polarimetric characteristics of melting hail at S and C bands. Preprints, *34th Conf. on Radar Meteorology*, Williamsburg, VA, Amer. Meteor. Soc., 4A.6. [Available online at <http://ams.confex.com/ams/pdfpapers/155571.pdf>.]
- Sachidananda, M., and D. S. Zrnica, 1987: Rain rate estimates from differential polarization measurements. *J. Atmos. Oceanic Technol.*, **4**, 588–598.
- Schuur, T. J., A. V. Ryzhkov, D. S. Zrnica, and M. Schönhuber, 2001: Drop size distributions measured by a 2D video disdrometer: Comparison with dual-polarization radar data. *J. Appl. Meteor.*, **40**, 1019–1094.
- Steiner, M., and R. A. Houze Jr., 1997: Sensitivity of the estimated monthly convective rain fraction to the choice of Z–R relation. *J. Appl. Meteor.*, **36**, 452–462.
- , —, and S. E. Yuter, 1995: Climatological characteristics of three-dimensional storm structure from operational radar and rain gauge data. *J. Appl. Meteor.*, **34**, 1978–2007.
- Straka, J. M., D. S. Zrnica, and A. V. Ryzhkov, 2000: Bulk hydrometeor classification and quantification using polarimetric radar data: Synthesis of relations. *J. Appl. Meteor.*, **39**, 1341–1372.
- Tabary, P., G. Vulpiani, J. Gourley, R. Thompson, and O. Bousquet, 2009: Unusually high differential attenuation at C band: Results from a two-year analysis of the French Trappes polarimetric radar data. *J. Appl. Meteor. Climatol.*, **48**, 2037–2053.
- Tessendorf, S. A., L. J. Miller, K. C. Wiens, and S. A. Rutledge, 2005: The 29 June 2000 supercell observed during STEPS. Part I: Kinematics and microphysics. *J. Atmos. Sci.*, **62**, 4127–4150.
- Thurai, M., G. J. Huang, V. N. Bringi, W. L. Randeu, and M. Schönhuber, 2007: Drop shapes, model comparisons, and calculations of polarimetric radar parameters in rain. *J. Atmos. Oceanic Technol.*, **24**, 1019–1032.
- , V. N. Bringi, and P. T. May, 2010: CPOL radar-derived drop size distribution statistics of stratiform and convective rain from two regimes in Darwin, Australia. *J. Atmos. Oceanic Technol.*, **27**, 932–942.
- Ulbrich, C. W., 1983: Natural variations in the analytical form of the raindrop size distribution. *J. Climate Appl. Meteor.*, **22**, 1764–1775.

- Wang, Y., and V. Chandrasekar, 2009: Algorithm for estimation of the specific differential phase. *J. Atmos. Oceanic Technol.*, **26**, 2565–2578.
- Williams, E. R., S. A. Rutledge, S. G. Geotis, N. Renno, E. Rasmussen, and T. Rickenbach, 1992: A radar and electrical study of tropical “hot towers.” *J. Atmos. Sci.*, **49**, 1386–1396.
- Zipser, E. J., and K. R. Lutz, 1994: The vertical profile of radar reflectivity of convective cells: A strong indicator of storm intensity and lightning probability? *Mon. Wea. Rev.*, **122**, 1751–1759.
- Zrnica, D. S., N. Balakrishnan, C. L. Ziegler, V. N. Bringi, K. Aydin, and T. Matejka, 1993a: Polarimetric signatures in the stratiform region of a mesoscale convective system. *J. Appl. Meteor.*, **32**, 678–693.
- , V. N. Bringi, N. Balakrishnan, K. Aydin, V. Chandrasekar, and J. Hubbert, 1993b: Polarimetric measurements in a severe hailstorm. *Mon. Wea. Rev.*, **121**, 2223–2238.
- , T. D. Keenan, L. D. Carey, and P. May, 2000: Sensitivity analysis of polarimetric variables at a 5-cm wavelength radar in rain. *J. Appl. Meteor.*, **39**, 1514–1526.